Mycobactin Analogues with Excellent Pharmacokinetic Profile Demonstrate Potent Antitubercular Specific Activity and Exceptional Efflux-Pump Inhibition

Mousumi Shyam[1,2], Harshita Verma[2], Gourab Bhattacharje[3], Piyali Mukherjee[4,5], Samsher Singh[4,5], Sujit Kamilya[6], Pushpendu Jalani[10], Swetarka Das[10], Arunava Dasgupta[10], Abhishake Mondal[6], Amit Kumar Das[3], Amit Singh[4,5], Federico Brucoli[9], Claire Bagnéris[2], Rachael Dickman[8], Vinay N Basavanakatti[7], Patibandla Naresh Babu[7], Vadivelan Sankaran[7], Abhimanyu Dev[1], Barij Nayan Sinha[1], Sanjib Bhakta[2*] and Venkatesan Jayaprakash[1*]

[1]*Department of Pharmaceutical Sciences & Technology, Birla Institute of Technology, Mesra, Ranchi 835215 (Jharkhand), India*

[2]*Mycobacteria Research Laboratory, Department of Biological Sciences, Institute of Structural and Molecular Biology, Birkbeck, University of London, Malet Street, London WC1E 7HX, UK*

[3]*Department of Biotechnology, Indian Institute of Technology Kharagpur, Kharagpur 721302, India*

[4]*Department of Microbiology and Cell Biology,* [5]*Centre for Infectious Disease Research, Indian Institute of Science, CV Raman Avenue, Bangalore 560012, India*

[6]*Solid State and Structural Chemistry Unit, Indian Institute of Science, CV Raman Avenue, Bangalore 560012, India*

[7]*Advinus Limited, 21 & 22, Peenya Industrial area, 560058, Bengaluru, India*

[8]*Pharmaceutical and Biological Chemistry, UCL School of Pharmacy, University of London, London WC1N 1AX, UK*

[9]*Leicester School of Pharmacy, De Montfort University, The Gateway, Leicester LE1 9BH, UK*

[10]*Microbiology Division, CSIR-Central Drug Research Institute, Sector 10 Janakipuram Extension, Sitapur Road, Lucknow 226031, India*

*Corresponding Authors contributed equally.

VJ: Email: venkatessanj@bitmesra.ac.in; Tel: +91-9470137264

SB: Email: s.bhakta@bbk.ac.uk /sanjib.bhakta@ucl.ac.uk; Tel: +44-2076316355

ABSTRACT:

In this study, we have designed and synthesized pyrazoline analogues that partially mimic the structure of mycobactin, to address the requirement of novel therapeutics to tackle the emerging global challenge of antimicrobial resistance (AMR). Our investigation resulted in the identification of novel lead compounds **44** and **49** as potential mycobactin biosynthesis inhibitors against mycobacteria. Moreover, candidates efficiently eradicated intracellularly surviving mycobacteria. Thermofluorimetric analysis and molecular dynamics simulations suggested compounds **44** and **49** bind to salicyl-AMP ligase (MbtA), a key enzyme in the mycobactin biosynthetic pathway. To the best of our knowledge, these are the first rationally designed mycobactin inhibitors to demonstrate an excellent *in vivo* pharmacokinetic profile. In addition, these compounds also exhibited more potent whole-cell efflux pump inhibition than known efflux pump inhibitors verapamil and chlorpromazine. Results from this study pave the way for the development of 3-(2-hydroxyphenyl)-5-(aryl)-pyrazolines as a new weapon against superbug associated AMR challenges.

Keywords: pyrazolines; mycobactin analogues; antitubercular; X-ray crystallography; intracellular killing; MbtA; thermofluor assay; pharmacokinetic profile; molecular dynamics simulation; efflux-pump inhibition.

INTRODUCTION

In early 1990s, the World Health Organization (WHO) first declared tuberculosis (TB) a global health emergency due to the emergence of drug-resistant TB[1]. Unfortunately in the last 20 years,[2] the world has continued struggling to control the severity of multidrug (MDR),[3,4,5] extensively drug (XDR),[6,7] and totally drug resistant (TDR)[8] TB cases. This underscores the urgent need for new chemotherapeutics with a novel mechanism of action.

In this context, the biosynthetic pathway of the conditionally essential mycobactin, a membrane-associated small molecule siderophore uniquely present in the *Mycobacterium* genus, offers a very promising avenue for therapeutic development against TB.[9,10,11] Mycobactin biosynthetic processes are not only restricted to the causative agent of TB, *Mycobacterium tuberculosis* (*Mtb*), but they are also present in *Mycobacterium smegmatis*, a non-pathogenic, fast-replicating species, and in non-tuberculous mycobacteria (NTM), which are opportunistic lung pathogens such as *Mycobacterium avium* and *Mycobacterium abscessus*.[12,13] The iron stress conditions encountered by mycobacteria within host macrophages instigates production of siderophores. Mycobactin (intracellular siderophore) and carboxymycobactin/exochellin (hydrophilic, extracellular siderophore) chelate iron from host iron-proteins and internalize this key trace element to support the essential bio-machineries of the mycobacteria.[14,15] The mycobactin megasynthase cluster is comprised of fourteen conditionally essential genes (*mbtA-mbtN*) encoding a mixed non-ribosomal peptide synthetase-polyketide synthetase (NRPS-PKS) system, and is responsible for the biosynthesis of mycobactin.[16] In the mycobactin megasynthase gene cluster, the bimodular system comprising the key enzymes salicyl-AMP ligase (MbtA) and phenyloxazoline synthetase (MbtB) is responsible for the development of the heterocyclic oxazoline segment of the mycobactin structure (**Figure 1**). MbtA catalyzes the first step of mycobactin biosynthesis in two-half reactions: First, MbtA promotes the activation of the salicylic acid with formation of salicyl-adenosine monophosphate (Sal-AMP), subsequently MbtA transfers Sal-AMP onto the phosphopantetheinylation (ppant) domain of MbtB, an acyl carrier protein, which is the MbtA-adjoining enzyme in the NRPS-PKS cluster.[17] The resulting MbtB-bound salicyl-thioester is then condensed with serine, which has been attached to the C-terminal ppant site of MbtB, to form an amide. The amide is cyclized to give rise, after few steps, to the 2-hydroxyphenyloxazoline nucleus of the mycobactins. MbtB oversees the cyclisation of both oxazoline and methyl-oxazoline, which leads to mycobactins T, N, and M. The MbtA-MbtB bimodular system, which is part of an essential and conserved biochemical machinery used by

pathogenic mycobacteria species to survive under iron-deficient conditions within host macrophages, is a promising therapeutic target in the battle against TB.[18]

In the last two decades several strategies have been adopted to target the mycobactin megasynthase protein cluster, and a number of targeted inhibitors were developed as antitubercular agents, as recently reviewed by our group.[19] In particular, since the early 2000s major research investigations have been focused around nucleoside analogues as MbtA-targeted inhibitors.[17a] On the other hand, we directed our efforts in identifying non-nucleoside probes that might interact with either adenylase or phenyloxazoline synthetase enzymes, and disrupt mycobactin biosynthesis. As a result, 3-(2-hydroxyphenyl)-5-(4-hydroxyphenyl)-4,5-dihydro-1*H*-pyrazole-1-carbothioamide (**1**) was designed and developed in 2008[20] and this compound represents the reference ligand for the current study. This hydoxyphenyl-pyrazole analogue (**1**) exhibited markedly higher anti-tubercular activity against *M. tuberculosis* strains cultured under iron-deprived (GAST) environments compared to mycobacteria grown in iron-rich (GAST-Fe) media.

Here, in continuation with our previous findings, we have integrated multidisciplinary approaches including rational structure-based mycobactin analogue design, chemical synthesis, whole-cell phenotypic and target-based evaluation and *in vivo* pharmacokinetic parameter profiling, to optimize the 2-hydroxyphenylpyrazolecarbothioamide scaffold and identify second-generation hit-compounds that can be considered as new anti-TB drug leads for further development (**Figure 1**).

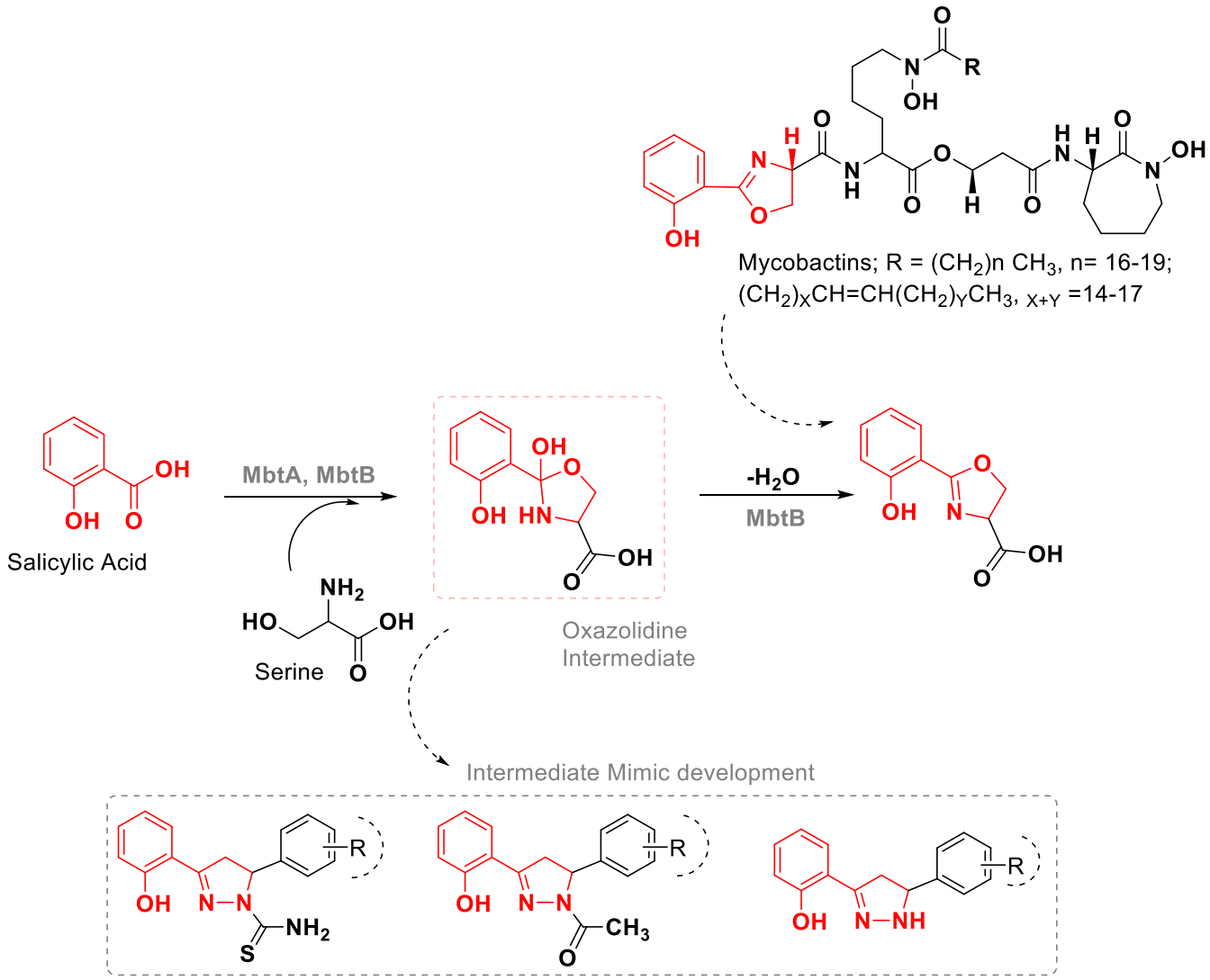

Figure 1. Intermediate mimic development to target the mycobactin biosynthetic pathway.

RESULTS AND DISCUSSION

Chemical Synthesis & Characterization.

Inspired by the encouraging antitubercular activity of our reference compound (**1**, compound *32* in our previous study),[20] structural explorations around the chemical space of its 2-hydroxyphenylpyrazolecarbothioamide framework was performed in this current study. The compound **1** scaffold is comprised of a 2-hydroxyphenyl unit (ring A) attached to the C3 position of a pyrazoline ring (ring B), which in turn is linked via its C5 position to a variously decorated aryl moiety (ring C). The pyrazoline nitrogen of compound **1** is capped with a thioamide group. **Scheme 1** illustrates the synthetic strategy for the preparation of analogues of compound **1**, which all retained the parent compound 2-hydroxy functional group in ring A, but carried different substitutions at ring C with the ring B nitrogen-bearing either an acetyl

group or a proton. This resulted in three different series of pyrazoline molecules (**2-49**), which were grouped in three libraries: Library 1 (**2-14**), 2 (**15-33**) and 3 (**34-49**).

All compounds were synthesized from substituted 2'-hydroxychalcones following the procedures reported earlier by our group (**Scheme 1**).[20-21] Hydroxychalcones were prepared through Claisen-Schmidt condensation of 2'-hydroxyacetophenone with appropriately substituted benzaldehydes in the presence of sodium hydroxide to give C1-C19. Library 1, which included the first series of carbothioamide pyrazoline derivatives (**1-14**) was obtained by condensing 2′-hydroxy chalcones C1-C12, C16 and C19 with thiosemicarbazide in alkaline medium. Library 2, which included the second series of *N*-acetyl pyrazolines derivatives (**15-33**), was obtained by condensing 2′-hydroxy chalcones C1-C19 with excess hydrazine hydrate in acetic acid. Library 3, which included the third series of *N*-H (unsubstituted) pyrazoline derivatives (**34-49**), was prepared by condensing 2′-hydroxy chalcones C1-C5, C7-C10, C12, C13, C15-C19 with 85% hydrazine hydrate in ethanol.

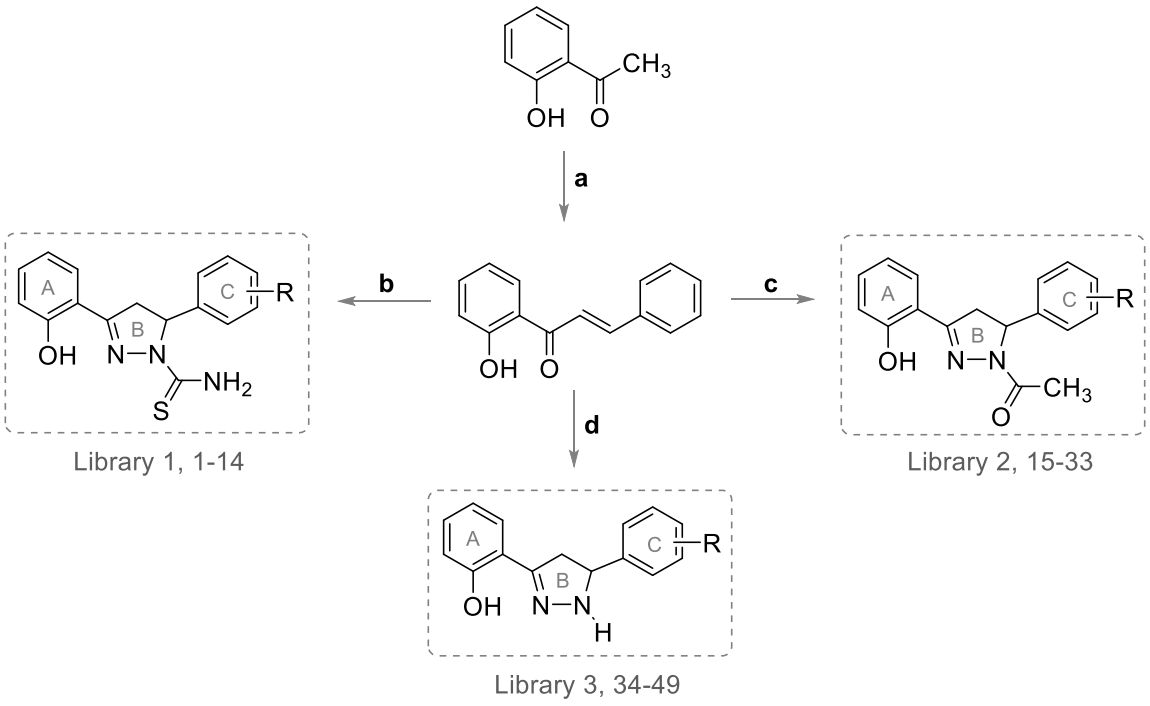

Reagents & Conditions: (a) (i) R-C_6H_4CHO, Aq. NaOH (60%), 0-5 °C, rt, 48 h; (ii) HCl (ice-cold, adjust pH to 2); (b) $H_2NC(S)NHNH_2$, KOH, reflux 8-10 h, (ii) HCl (ice-cold, adjust pH to 2); (c) NH_2NH_2, glacial CH_3COOH, reflux, 6 h. (d) NH_2NH_2, EtOH, reflux, 6 h.

Scheme 1: Synthesis of substituted pyrazolines

Chalcone intermediates (C1-C19) were characterized by comparing their melting points with the reported value (Supporting Information: Physico-chemical characteristics of compounds C1-C19, Table S1). All novel compounds were characterized by ^{1}H-NMR, ^{13}C-NMR, ESI-MS and HRMS (Supporting Information: ^{1}H-NMR, ^{13}C-NMR, ESI-MS and HRMS spectra of analogues (**1**-**49**)).

Mode(s) and Molecular Mechanism(s) of Antibiotic Action:

Antitubercular activity in iron-rich and iron-deprived media.

Library 1 members, which included fourteen *N1*-carbothioamide pyrazolines (**1-14**), were evaluated for their antimycobacterial activity in iron-rich GAST-Fe and iron-deprived GAST medium using *M. smegmatis* (mc^2 155, ATCC 700084) and *M. tuberculosis* (H37Rv, ATCC 27294) strains (Table 1). Compounds **1**, **3**, and **8** were already reported by our group[21] and were re-tested for comparative purposes. Library 1 compounds were not active against *M. smegmatis*, but exhibited anti-tubercular activity against *M. tuberculosis*. Compound **2**, which contained an unsubstituted phenyl unit (ring C) attached to the C-5 position of the pyrazoline ring (ring B), was found to be the most potent amongst the fourteen Library 1 molecules with a MIC_{90} value of 4 µg/mL and 128 µg/mL in GAST and GAST-Fe media, respectively, and with a Target Selectivity Index (TSI) of 32. TSI is the ratio of MIC_{90} in GAST-Fe media to MIC_{90} in GAST media. TSI differs from Selectivity Index (SI), which is the ratio of host cell cytotoxic concentration to pathogen's inhibitory concentration. The remarkable efficacy of compound **2** against *M. tuberculosis* colonies cultured in iron-depleted media (GAST) strongly suggested that this pyrazoline analogue might be targeting conditionally-essential enzymes expressed under iron-deprived environments. The second most potent compound in this series was **4** (considering the highest TSI rather than the lowest MIC value). A close inspection allowed us to reveal the substitutional difference between **4** and **2** is a hydroxy substitution at the 3rd position of phenyl ring C. It is worthwhile noting that any substitutions introduced in ring C were found to decrease the anti-tubercular activity of this series of compounds. This is probably due to steric clashes at the binding site rather than electronic effects of the substituents, as both electron-donating and -withdrawing groups in ring C were found to reduce the anti-mycobacterial activity of Library 1 members as compared to analogue **2**, which contained an unsubstituted ring C. A report by McMahon *et al.* (2012) suggests that the Adenylation (A) domain of MbtB has preference for threonine and indicates the presence of a pocket in the cyclization (Cy) domain of MbtB to accommodate the C5-methyl group of the

oxazoline intermediate that is appended to the thiolation region of the enzyme[22] (**Figure 2**). According to our experimental data based on the structure-activity-relationship (SAR) of Library 1 compounds, we postulated that the volume of this pocket must be sufficient enough to accommodate a phenyl ring (ring C), but not substituted phenyl moieties, resulting in compounds devoid of bactericidal activity and narrow TSI, possibly due to their inability to bind to the enzymatic target.

Table 1. Antitubercular activity of compounds **1-14** in GAST and GAST-Fe media against *M. smegmatis* and *M. tuberculosis*.

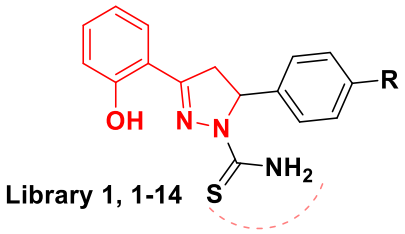

Code	R	MIC$_{90}$ (µg/mL) *M. smegmatis*		TSI	MIC$_{90}$ (µg/mL) *M. tuberculosis*		TSI
		GAST	GAST-Fe		GAST	GAST-Fe	
1[a]	4-OH	256	>256	>1	64	256	4
2	H	128	256	2	4	128	32
3[b]	2-OH	64	256	4	256	256	1
4	3-OH	128	256	2	16	128	8
5	2-OCH_3	256	>256	>1	16	16	1
6	3-OCH_3	>256	>256	-nd-	32	64	2
7	4-OCH_3	128	>256	>2	64	>256	4
8[b]	2-CH_3	128	256	2	16	16	1
9	4-CH_3	128	256	2	8	8	1
10	3-OH, 4-OCH_3	128	128	1	8	16	2
11	2-Cl	256	256	1	8	16	2
12	3-Cl	256	256	1	16	32	2
13	4-Cl	128	256	2	4	8	2
14	2-F	128	128	1	16	32	2

[a] Stirrett *et al.* 2008,[20] **b** Ferreras *et al.* 2011.[21] Conc. for pyrazoline derivatives was in the range of 256-0.125 µg/mL; nd, not determined; '>', when MIC conc. was obtained beyond the maximum limit (256 µg/mL) of test concentration

Compounds of Library 2 (Table 2) were designed by using the concept of bioisosteric replacement. Oxygen was used as a divalent isostere for the thiocarbomoyl S and a methyl group as a monovalent Grimm's hydride isostere for the amino group to obtain the acetyl derivatives. Two acetyl derivatives **16** & **18** (compounds coded **3** & **4** from Ferreras *et al.* 2011[21]) reported earlier by our group revealed that acetyl group substitution at the *N1* position

did not provide target selectivity towards conditionally essential targets in the iron acquisition pathway. Since the chemical space around the phenyl ring at 5th position of pyrazoline was not explored in detail with enough analogues, we designed Library 2. To understand the contribution of the sulfur atom present in *N1*-thioamide group towards anti-mycobacterial activity, this compound class was evaluated against *M. tuberculosis* and *M. smegmatis* in both iron-replete and depleted media. It was found that bioisosteric replacement of the thiocarbamoyl unit at ring B (pyrazoline) *N1* with an acetyl group led to compounds which were inactive against the bacterial strains cultured in both GAST and GAST-Fe conditions. As a result, it is apparent that a thioamide capping unit at the pyrazoline *N1* is an indispensable requirement for the biological activity of this class of compounds and presumably for binding to the binding pocket of the MbtB cyclization domain. A probable thioamide-iminothiol tautomerism in pyrazoline analogue **2** might lead to the generation of a structure that mimics part of the thioester bond linking the 2-hydroxyphenyl intermediate to the MbtB thiolation domain (**Figure 2**). This structural mimic cannot be formed with Library 2 pyrazoline compounds bearing an *N1*-acetyl group.

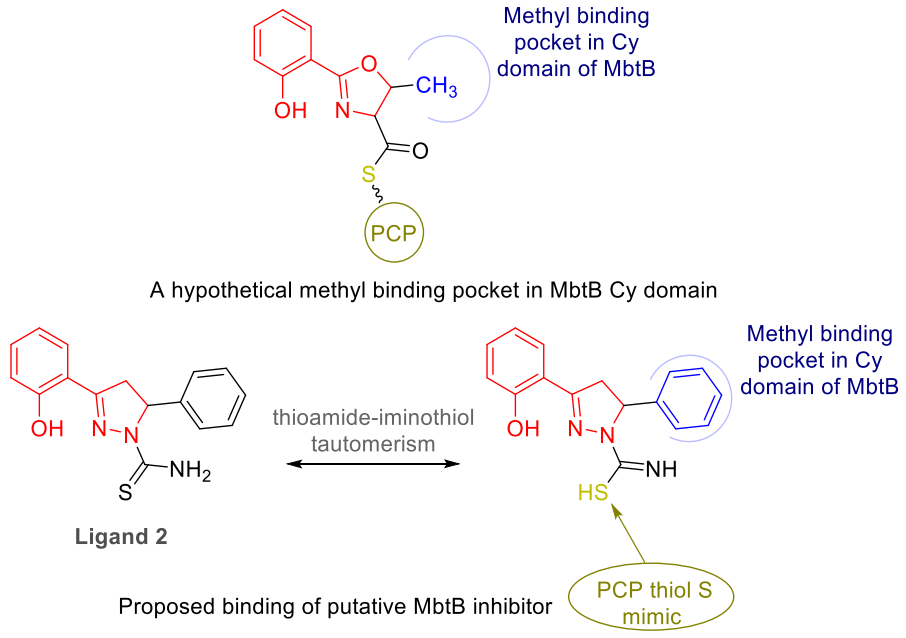

Figure 2. Hypothetical model for inhibition of MbtB Cyclization domain by compound **2**, PCP-peptidyl carrier protein domain.

Table 2. Antitubercular activity of compounds **15-33** in GAST and GAST-Fe media against *M. smegmatis* and *M. tuberculosis*.

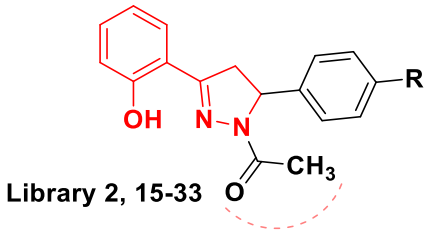

Code	R	MIC$_{90}$ (μg/mL) *M. smegmatis*		TSI	MIC$_{90}$ (μg/mL) *M. tuberculosis*		TSI
		GAST	GAST-Fe		GAST	GAST-Fe	
15	H	>256	>256	-nd-	>256	>256	-nd-
16[b]	2-OH	>256	>256	-nd-	>256	256	-nd-
17	3-OH	>256	>256	-nd-	>256	>256	-nd-
18[b]	4-OH	>256	>256	-nd-	>256	>256	-nd-
19	2-OCH_3	>256	>256	-nd-	>256	>256	-nd-
20	3-OCH_3	>256	256	-nd-	>256	>256	-nd-
21	4-OCH_3	>256	>256	-nd-	>256	>256	-nd-
22	3-OH, 4-OCH_3	>256	>256	-nd-	>256	>256	-nd-
23	2-CH_3	>256	256	-nd-	>256	256	-nd-
24	4-CH_3	>256	256	-nd-	>256	>256	-nd-
25	2-Cl	>256	256	-nd-	>256	>256	-nd-
26	3-Cl	128	128	1	256	>256	>1
27	4-Cl	>256	256	-nd-	>256	>256	-nd-
28	2-F	256	256	1	>256	>256	-nd-
29	3-F	128	128	1	64	256	4
30	4-F	128	128	1	128	256	2
31	2-Br	>256	>256	-nd-	>256	>256	-nd-
32	3-Br	>256	256	-nd-	>256	>256	-nd-
33	4-Br	>256	>256	-nd-	>256	>256	-nd-

[b]Ferreras *et al.* 2011.[21] Conc. for pyrazoline derivatives was in the range of 256-0.125 μg/mL; nd, not determined; '>', when MIC conc. was obtained beyond the maximum limit (256 μg/mL) of the test concentration

In order to further explore SAR around ring B (pyrazoline ring) *N1*, a 16-member (**34**-**49**) library (Library 3, Table 3) was synthesized and tested for anti-tubercular activity in GAST and GAST-Fe media. To our surprise, compounds from this series displayed activity as well as target selectivity in both *M. smegmatis* and *M. tuberculosis*. Compound **34**, which is an *N1*-unsubstituted analogue of **2**, was found to be H37Rv-active with a TSI of 4 and MIC$_{90}$ value of a 32 μg/mL, although showing a 8-fold reduced potency compared to **2**. In contrast to Library 1 results, substitutions on ring C (e.g., phenyl ring at C5 position of pyrazoline) were tolerated and, in some cases, resulted in significant improvement of anti-tubercular activity in low-iron media. For example, analogues **44**, **47** and **49** including electronegative atoms (e.g., -Br, -Cl, -

F) at C4 of ring C exhibited notable activity against *M. tuberculosis* in iron-impoverished media with MIC_{90} values of 16 (**44**, **47**) and 8 μg/mL (**49**) and favorable TSI scores (8 for analogues **44** and **47**, and 16 for analogue **49**). Conversely, it was found that electron-donating groups (*e.g.*, -OH, $-OCH_3$ and $-CH_3$) in ring C reduced both mycobacterial growth inhibitory properties and target selectivity (*i.e.*, iron-rich *vs* iron-deprived environment) of Library 3 compounds. The latter findings, which are related to Library 3 compounds, are somehow contradictory to the theory we have previously formulated to explain Library 1 member's anti-tubercular activity and MbtB-target selectivity profile. Our hypothesis took into consideration the following points:

i) the presence of a pocket in the MbtB Cy domain sufficiently large to accommodate an unsubstituted phenyl ring (ring C) and

ii) Thioamide-iminothiol tautomerism generating mimic structures resembling part of the MbtB-bound oxazoline intermediate that will grow into the mycobactins core.

Although a certain answer cannot be found at this stage, it can only be assumed that Library 3 compounds, which mainly differ from Library 1 analogues for the absence of a thioamide capping unit at *N1* of ring B, might be targeting enzymatic processes involved in iron acquisition and, more specifically, other enzymes of the mycobactin biosynthetic pathway. Considering the simplicity of the structure of Library 3 compounds, we postulated that these unsubstituted pyrazoline derivatives may interact with MbtA, the gateway enzyme of the mycobactin synthetic pathway. As can be noted in **Figure 3**, the 3-(2-hydroxyphenyl)-*N1H*-pyrazoline unit mimics the structure of salicylic acid, which is a substrate of MbtA. In addition, pyrazoline N-H can be regarded as a bioisosteric equivalent of the carboxylic acid functional group.[23]

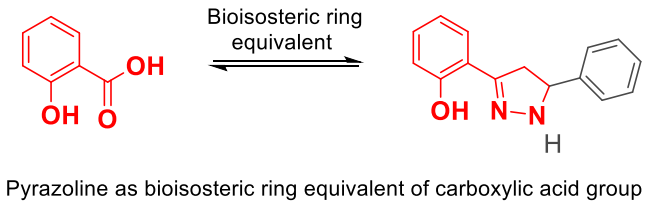

Figure 3. Structural similarity between salicylic acid and the 3-(2-hydroxyphenyl)-N1*H*-pyrazoline unit of Library 3 compounds **44** and **49**.

Table 3. Antitubercular activity of Library 3 compounds **34**-**49** in GAST and GAST-Fe media against *M. smegmatis* and *M. tuberculosis*.

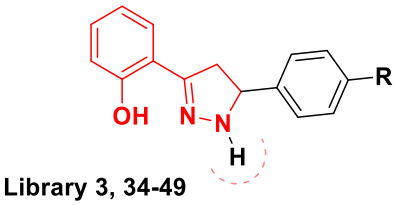

Library 3, 34-49

Code	R	MIC$_{90}$ (µg/mL) *M. smegmatis*		TSI	MIC$_{90}$ (µg/mL) *M. tuberculosis*		TSI
		GAST	GAST-Fe		GAST	GAST-Fe	
34	H	64	128	2	32	128	4
35[b]	2-OH	64	64	-nd-	64	>256	>4
36	3-OH	64	64	-nd-	64	>256	>4
37[b]	4-OH	32	64	2	128	>256	>2
38	2-OCH_3	64	128	2	32	256	8
39	4-OCH_3	64	128	2	32	128	4
40	3-OH, 4-OCH_3	>256	>256	-nd-	128	256	2
41	2-CH_3	16	128	8	16	64	4
42	4-CH_3	16	64	4	8	32	4
43	2-Cl	8	64	8	16	32	2
44	4-Cl	4	64	16	16	128	8
45	2-F	8	64	8	16	64	4
46	3-F	16	64	4	64	256	4
47	4-F	8	64	8	16	128	8
48	2-Br	8	64	8	16	32	2
49	4-Br	4	64	16	8	128	16
RIF		8	8	1	0.03	0.005	0.2
INH		2	2	1	0.03	0.005	0.2

bFerreras *et al.* 2011.[21] Conc. for pyrazoline derivatives and rifampicin (RIF), isoniazid (INH) was in the range of 256-0.125 µg/mL and 32-0.015 µg/mL respectively; nd, not determined; '>', when MIC conc. was obtained beyond the maximum limit (256 µg/mL) of test concentration

A number of Library 3 compounds displayed target selectivity against *M. smegmatis*. Therefore, it was decided to screen compounds **44** and **49** against *Mycobacterium aurum* (ATCC 10437) and *Mycobacterium bovis* BCG (Table 4). Analogues **1** and **2** were tested for comparative purposes and showed a narrow TSI (0-2) score that is indicative of a non-involvement in siderophore biosynthesis or iron acquisition processes in *M. bovis* BCG and *M. aurum*. On the other hand, compounds **44** and **49** exhibited growth inhibition activity against both *M. aurum* and *M. bovis* BCG in GAST (iron-deplete) media at a concentration as low as 8 µg/mL. The activity profile of these compounds is quite encouraging as they may be highly efficient in handling infection due to both pathogens and opportunistic pathogens under immunocompromised settings like HIV and organ transplantation.[24]

Table 4. Antimycobacterial activity of compounds **1**, **2**, **44** and **49**.

Code	MIC_{90} (µg/mL) *M. aurum*		TSI	MIC_{90} (µg/mL) *M. bovis* BCG		TSI
	GAST	GAST-Fe		GAST	GAST-Fe	
1	64	128	2	16	32	2
2	64	64	1	16	32	2
44	16	128	8	8	32	4
49	8	128	16	8	64	8

Conc. for pyrazoline derivatives was in the range of 256-0.125 µg/mL

Henceforth, considering compound **44** and **49** as the most promising candidates from this extensive SAR study, we carried forward our investigation to understand in depth the mode and mechanism of action along with additional evaluation of therapeutic potential of these lead candidates. Initially, we took steps towards understanding the topology of the lead candidates along with packing and intermolecular interactions in their crystal arrangements.

X-ray crystallography and Hirshfeld surface analysis of compounds *44* and *49*.

The structures of compounds **44** and **49** were investigated by X-ray crystallography. The ORTEP diagram and asymmetric unit representation are shown in **Figure 4**. Both compounds crystallized in the monoclinic space group $P2_1/n$. The crystallographic parameters are provided in the Supporting Information (X-ray crystallographic parameters of compounds **44** and **49**, **Table S2)**.

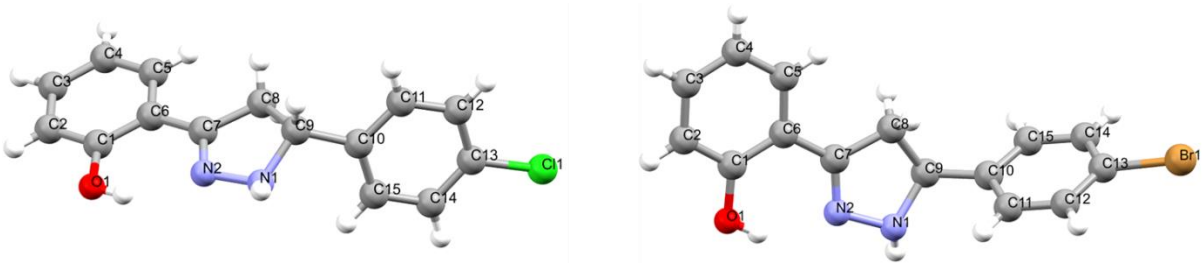

Figure 4. ORTEP diagram of compounds **44** and **49.**

Hirshfeld Surface (HS) analysis was performed and fingerprint plots were mapped to quantitatively study the intermolecular interactions of compounds **44** and **49** to identify the characteristic packing modes and ways in which the nearby molecules contact one another (**Figure 5** and **6**). Both the candidates belonged to the same chemical class and bore the same

general chemical features, although they differed in halogen substitution. HS mapping contributed towards identifying common interactions as well as specific contributions of each halogen in the overall crystal packing.

The di (distance from the HS to the nearest atom inside the surface), de (distance from the HS to the nearest atom outside the surface), and dnorm (normalized contact distance) indicate the distances from the nuclei to the HS, with respect to relative van der Waals radii. In the HS mapped over dnorm, the white surface designates contacts with distances equal to the sum of van der Waals radii, and the red and blue colours represent distances shorter or longer than the van der Waals radii. Fingerprint plots revealed that H···H (35.1% for **44**, 38.0% for **49**) and C···H (30.0% for **44**, 29.0% for **49**) were the two most prevalent atomic interactions observed in the lattices. Moreover, N···H (4.4% for **44**, 5.3% for **49**) and O···H (7.2% for **44**, 7.4% for **49**) interactions had a lesser contribution in the crystal arrangement of the molecules. However, Cl···H (14.5%) and Br···H (15.5%) interactions contributed more to the crystal lattice compared to weak N···H and O···H interactions.

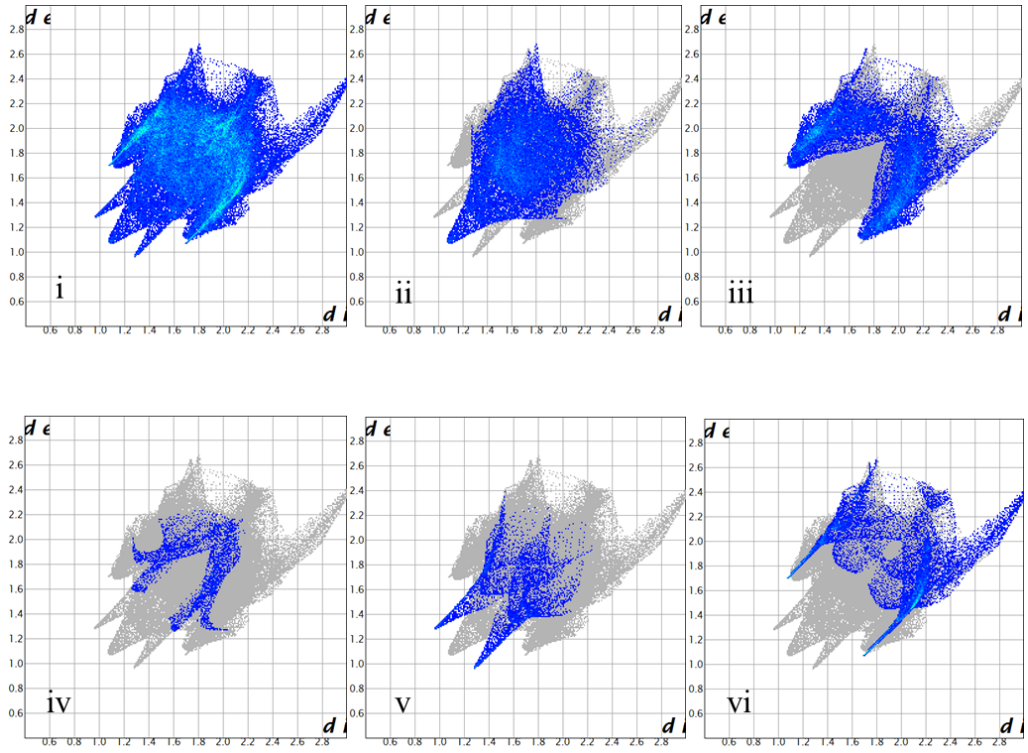

Figure 5. Hirshfeld Surface analysis of compound **44**. Fingerprint plots showing (i) all, (ii) H···H, (iii) C···H, (iv) N···H, (v) O···H, and (vi) Cl···H close contacts diagrams.

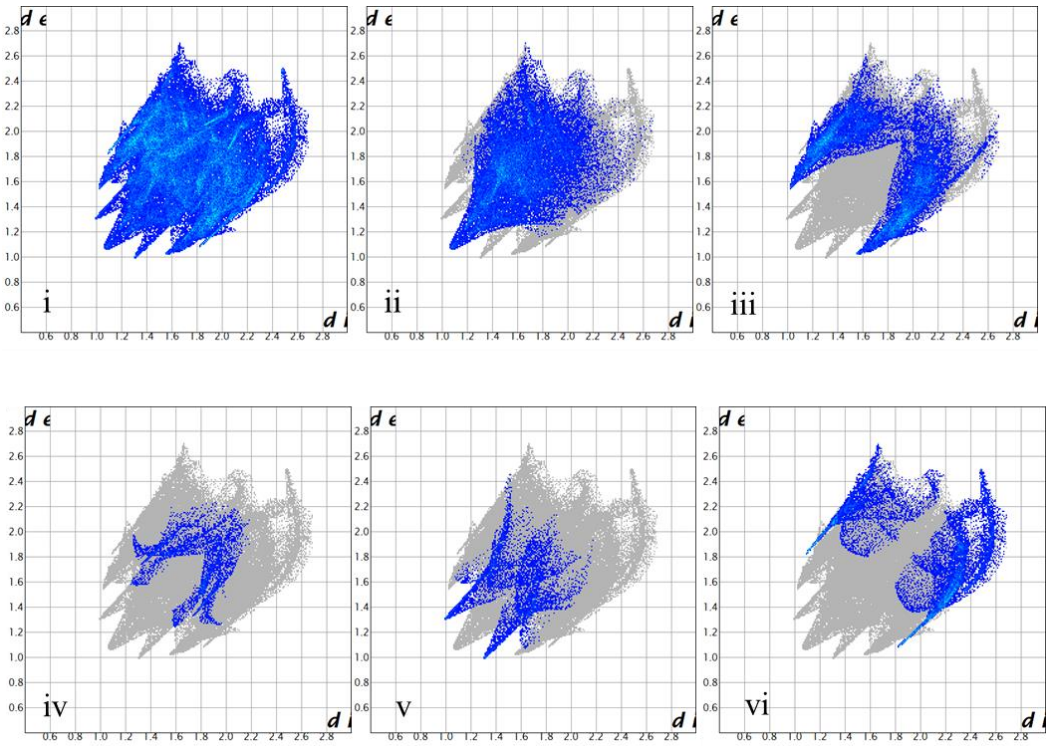

Figure 6. Hirshfeld surface analysis of compound **49**. Fingerprint plots showing (i) all, (ii) H···H, (iii) C···H, (iv) N···H, (v) O···H, and (vi) Br···H close contacts diagrams.

Investigating bacteriostatic growth inhibition *vs* bactericidal mode of killing.

Compounds **44** and **49** were further investigated for their bacteriostatic-bactericidal mode of action using the HT-SPOTi assay method with *M. smegmatis mc*^{2} *155* as the model.[25] The respective wells were first earmarked where the MIC of compounds **44** and **49** was determined. The entire surface of the well was scraped and inoculated in inhibitor-free culture media to monitor their growth over a period of five days. No growth was observed for the **44**-treated culture whereas the **49**-treated culture was resuscitated. Therefore, the modes of antimycobacterial action for **44** and **49** were inferred to be bactericidal and bacteriostatic respectively.

Estimation of siderophore production in presence of 44 and 49.

Compounds **44** and **49** were tested using the Universal CAS siderophore production assay in *M. smegmatis mc*^{2} *155* to ascertain whether the effects of the compounds were due to inhibition of biosynthesis of mycobactins. The biosynthetic pathway leading to the synthesis of mycobactins is common for both pathogens and opportunistic pathogens (non-pathogenic mycobacteria). Hence, fast growing *M. smegmatis* was selected as a suitable surrogate for *M. tuberculosis* in this assay.[26] The universal CAS assay uses a chrome azurol sulfonate (CAS),

iron(III), hexadecyltrimethylammonium bromide ternary complex which is blue in color. When a siderophore removes iron from the ternary complex, the color changes from blue to orange, providing an indirect measurement of siderophore production by the bacteria. Siderophore production under different iron stress conditions was first modelled using varying concentrations of iron supplemented medium (200 μM, 20 μM, 2 μM, and 0 μM) and assessing the reduction in optical density of the respective samples. Iron availability in media is inversely proportional to siderophore production, thus maximum optical density of CAS solution was observed for 200 μM iron supplemented media ($p < 0.001$) with respect to the control (minimal media) (**Figure 7a**). A comparison between media with 0 μM and 2 μM iron revealed that there was no significant difference between these two groups. Thus, the iron concentration range 0 - 2 μM can be considered as iron-limiting conditions and is likely to lead to the highest production of siderophores compared to the two other iron supplemented (20 and 200 μM) media studied here.

In the MIC determination assay we observed that lead compounds **44** and **49** exhibited MIC_{90} of 4 μg/mL in iron-deficient GAST medium against *M. smegmatis* (Table 3). We therefore estimated siderophore production in the presence of the lead compounds at 4 μg/mL (1 x MIC dose) at the 3 h time-point. This study indicated a more significant inhibition of siderophore production for **49** ($p < 0.01$) compared to **44** ($p < 0.05$) (**Figure 7b**). Siderophore production units calculated for candidates **44** and **49** were 54.70% and 51.76% respectively.

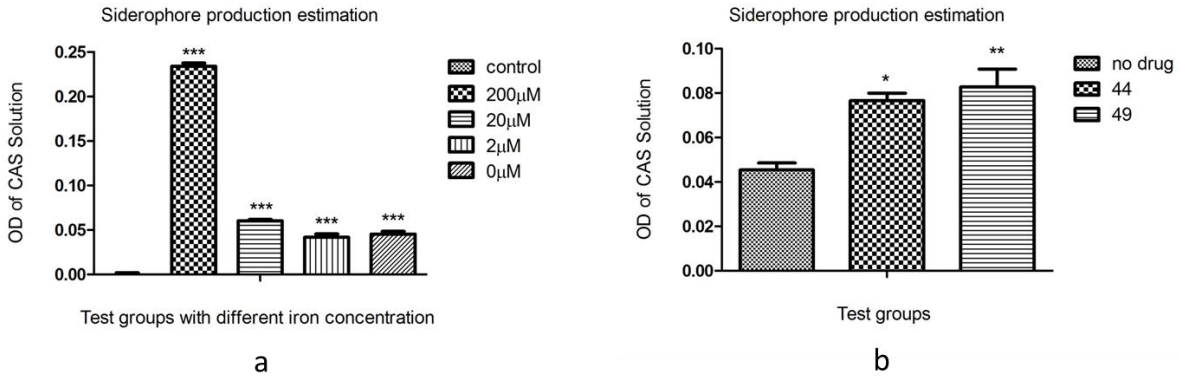

Figure 7. Siderophore production estimation in *M. smegmatis*. **a.** Estimation of siderophore production at different iron concentrations; **b.** siderophore inhibition in the presence of **44** and **49** at 1 x MIC dose concentration in *M. smegmatis*; 4 μg/mL for each compound. Data represented as Mean ± SEM, analysed by One-Way ANOVA followed by Bonferroni's multiple comparisons test. Significant: ns $p > 0.05$; *$p < 0.05$; **$p < 0.01$; ***$p < 0.001$.

Biochemical Investigation using Thermofluorimetry.

As previously mentioned, it was postulated that the *o*-hydroxyphenyl moiety of pyrazoline analogues **44** and **49** might be a structural requirement for binding to both MbtA and MbtB. Therefore, we attempted the heterologous expression and purification of the full length recombinant MbtA, MbtB from *M. tuberculosis* as well as the Cy domain of the Mtb-MbtB protein since that specific domain of MbtB is thought to be responsible for the cyclisation of Salicyl-AMP and serine to produce the cyclized oxazoline intermediate. Unfortunately, we were unable to produce enough soluble proteins of the tubercle bacilli to carry out any biochemical studies. All design strategies and respective findings are provided in the Supporting Information (Molecular Biology: Expression and Purification of Bimodular System). We therefore expressed and purified[27] recombinant protein MbtA from *M. smegmatis* and investigated the effect of compounds **44** and **49** on the thermal stability of MbtA by carrying out a thermal shift assay (**Figure 8-9**).[28,29]

Prior to testing the ligands, the thermal stability of the MbtA protein was tested at different pH (6.5, 7.5, and 8.5) and NaCl concentration (100 mM and 500 mM). Two melting temperatures (T_m) for MbtA were observed when using the different buffer conditions but it appeared to be more noticeable at pH 6.5 100 mM NaCl and 500 mM NaCl, and at pH 7.5 and pH 8.5 using the lower 100 mM NaCl (**Figure 8**). The second higher T_m was however too broad to be measured accurately and therefore, only the first lower T_m is displayed (**Figure 8b**). Two T_ms could be revealing the denaturation of two different domains, one being more stable than the other. Further, the first T_m increases as the pH value and NaCl concentration increase: 35°C for 100 mM and 500 mM NaCl at pH 6.5; 41°C for 100 mM NaCl pH 7.5, and 41.5°C for 100 mM NaCl pH 8.5; and finally, 44°C for 500 mM NaCl pH 7.5 and 44.5°C for 500 mM NaCl pH 8.5. This shift in T_m reveals a stabilization of MbtA at high pH and high concentration of salt. Under these conditions, it also appeared that the second T_m blends into the first T_m, potentially indicating the presence of a tighter conformation of both domains in MbtA. The overall structure of MbtA consists of one large N-terminal domain (1-457) encompassing most of the protein linked through a short hinge to a second smaller tight C-terminal domain (458-558).[30] Structural studies from other proteins possessing similar enzyme activities and about 40% sequence identity have shown the second domain to harbor different conformations relative to the main domain when in the presence of substrates or in their apo forms, indicating this domain to form a highly flexible "lid" implicated in enzyme/substrate catalysis.[31,32] Therefore, the presence of these two flexible domains could explain the presence of two T_m values, especially in an environment favoring destabilization of the protein, i.e. lower pH and salt concentration.

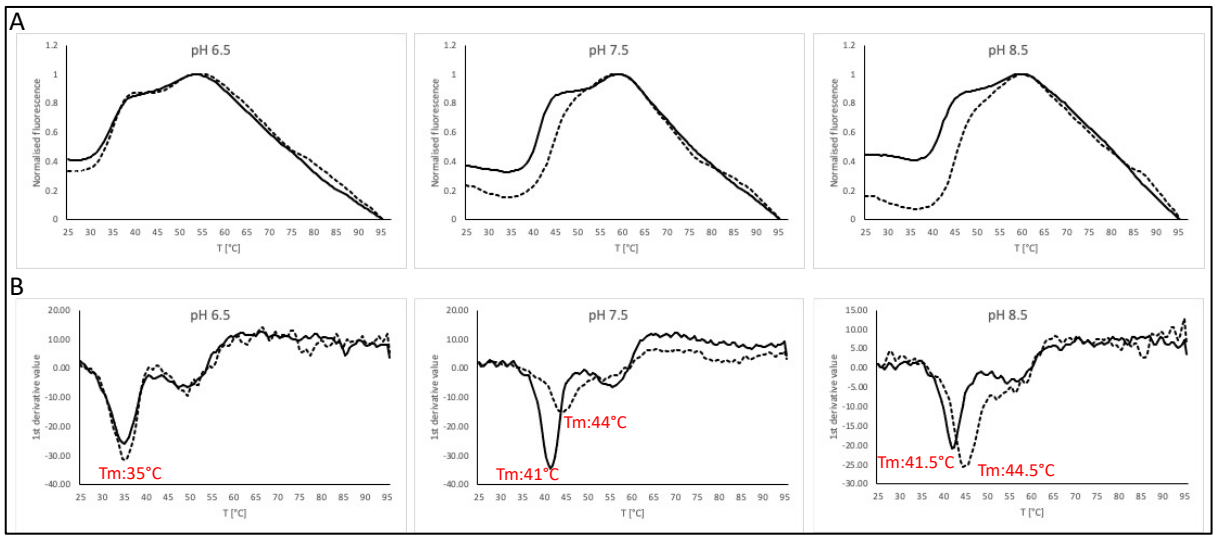

Figure 8. **a.** Normalised thermal shift plots of MbtA at different pH and NaCl concentration (100 mM, full line; 500 mM, dashed line). The melting temperature (T_m) corresponds to the inflection point on the rising curve. **b.** First derivative plots displaying troughs corresponding to the T_m in (A). Two T_ms are visible, however, only the first T_m value is displayed in red since the second T_m trough is too broad to obtain an accurate measurement.

Furthermore, since the ligands to be tested are solubilized in 1% DMSO, the effect of DMSO alone on MbtA thermal stability was tested and was found not to induce a shift in T_m (data not shown). Finally, MbtA thermal shift curves were recorded in the absence (1% DMSO only) and in the presence of ligands **1**, **44**, and **49** at a concentration of 100 µM using the buffers that were shown to stabilize MbtA. A shift of 2 °C was recorded for both ligands **44** and **49** when using 100 mM NaCl at pH 7.5 and 2 °C and 2.5 °C when using 100 mM NaCl at pH 8.5 for ligands **44** and **49** respectively (**Figure 9**). This result is in accordance with the study conducted by Fergusson et al.,[27] where they observed similar shifts upon ligand binding. A less dramatic T_m shift of 0.5 °C was observed under the two higher pHs and 500 mM NaCl buffer conditions for ligand **44** and **49** when MbtA is in its more stable environment (Supporting Information: Study of the effect of ligands **1**, **44**, and **49** on MbtA thermostability compared to the control 1% DMSO). Ligand **1** did not seem to affect the T_m under the buffer conditions used in this study, as expected for compound from Library 1 might have different a target binding site other than MbtA.

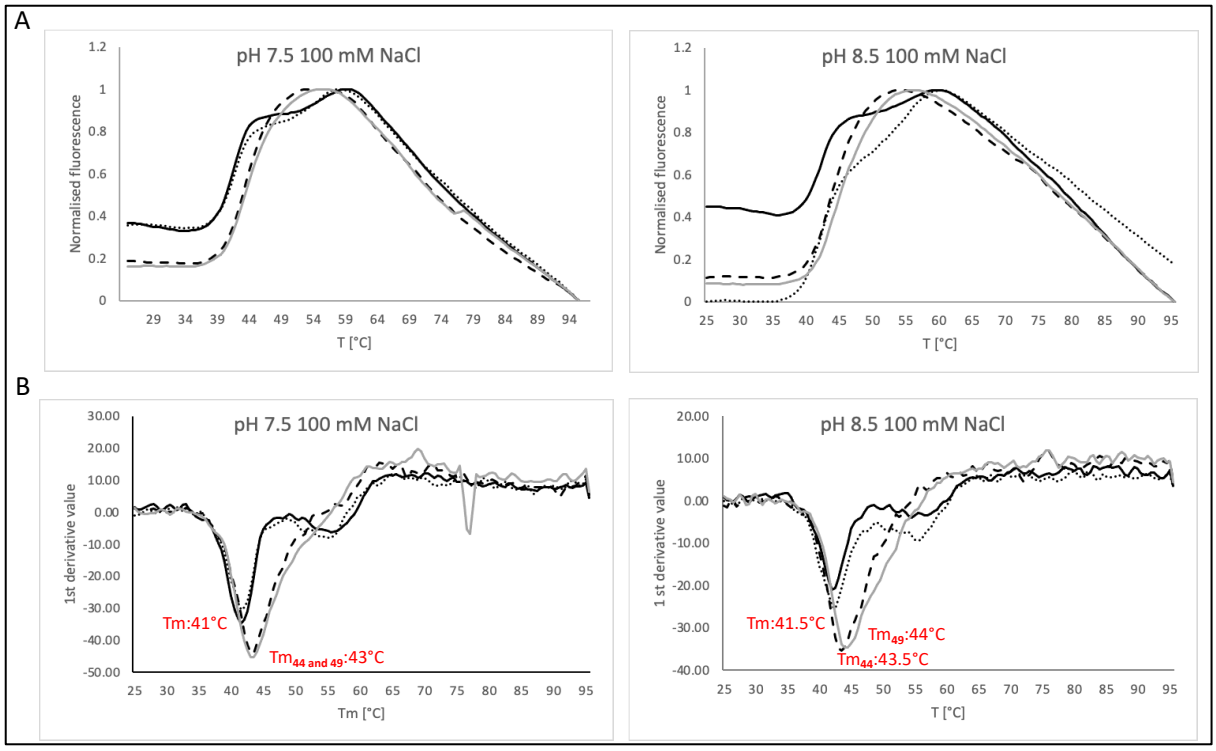

Figure 9. Study of the effect of ligands **1** (dotted line), **44** (dashed line), **49** (grey line) on MbtA thermostability compared to the control 1% DMSO (full line) using two buffers containing 100 mM NaCl at either pH 7.5 or pH 8.5. **a.** Normalised thermal shift plots. The melting temperature (T_m) corresponds to the inflection point on the rising curve. **b.** First derivative plots displaying troughs corresponding to the T_m in (**a**). Only the first T_m value is displayed in red since the second T_m trough is too broad to obtain an accurate measurement.

Molecular dynamics simulations of MbtA-44 and MbtA-49 complexes.

In an effort to understand the interactions of **44** and **49** with MbtA, we ran 50 ns molecular dynamics simulations using GROMACS. Protein-inhibitor complexes MbtA-**44** and MbtA-**49** (**Figure 10**) required for the dynamics simulations were obtained by molecular docking with the X-ray crystal structure of MbtA from *M. smegmatis* (PDB ID: 5KEI, 2.33Å)[17b] using AutoDock 4.2 (Supporting Information: Molecular Docking Study Analysis).

It should also be noted that protein lysine acyltransferase (Pat) and deacetyltransferase (DAc) regulate MbtA catalytic activity through reversible acetylation and deacetylation at Lys546 of MbtA.[30] We can hypothesize that binding of both the ligands **44** and **49** (**Figure 10**) at the Lys546 centered catalytic pocket present in the C-terminal domain may restrict the substrate binding which inhibits the enzymatic function of MbtA.

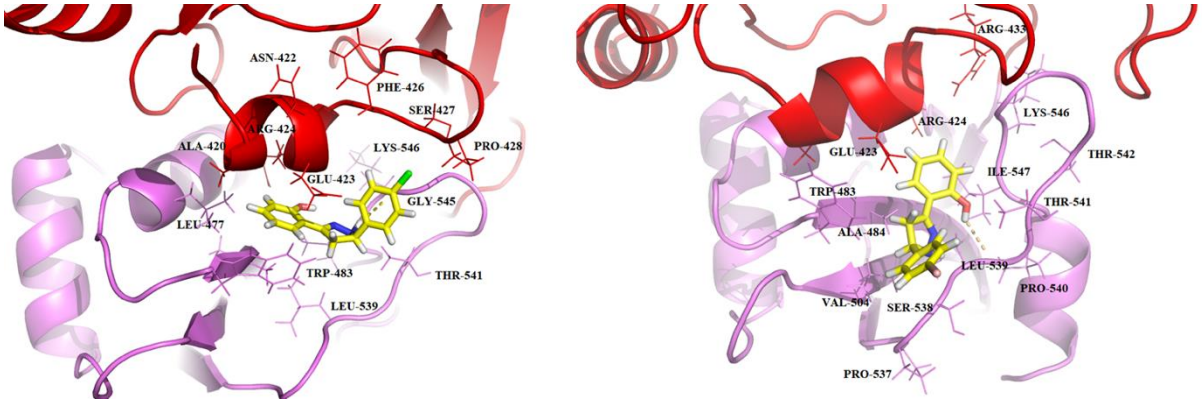

Figure 10. 3D Interactions of **44** and **49** with the active site of MbtA (PDB: 5KEI) in the docked complexes after 50 ns simulation. Dotted lines indicate hydrogen bonding with MbtA residues.

Root mean square deviation (RMSD) analyses showed that the protein backbone stabilized for all the three systems after ~20 ns with RMSD around 0.25 nm (**Figure 11a**). Differences in RMSD values between the three systems revealed that the backbone of MbtA is relatively more stable in the protein-ligand complexes than in the apo-protein. No major structural changes were observed for both the ligands during the simulation (**Figure 11**). Root mean square fluctuation (RMSF) of a group of atoms extracted from MD indicates their overall conformation mobility. A plot of RMSF *vs* time indicated higher mobilities for N and C terminal residues and the loop regions of MbtA for all the three systems (**Figure 11b**). A plot of radius of gyration (R_g) *vs* time suggested a relatively extended structure for MbtA-**44** and compact structure for MbtA-**49** (**Figure 11c**). A plot of number of intermolecular hydrogen bonds *vs* time revealed 0-2 hydrogen bonds for the MbtA-**44** complex after 20 ns, while for MbtA-**49** at least 3 hydrogen bonds were found after 30 ns (**Figure 11d, 11e**). The MbtA-**44** complex exhibited hydrogen bonding interactions with Ala420, Glu423 and Gly545, while for MbtA-**49** it was with Arg424, Arg433, and Gly545. Further, trajectories from the last 10 ns of the simulations were used to calculate the estimated binding free energy (EBFE) with snapshots from every 50 ps using Molecular Mechanics Poisson Boltzmaan Surface Area (Supporting Information: MMPBSA Study and Analysis). **Table 5** summarizes the contributions of various non-covalent interactions that stabilize the protein-ligand complexes. It can be observed that total binding free energy remains negative for both MbtA-**44** and MbtA-**49**, indicating stable complexes between the ligands **44** and **49** and the protein MbtA (**Figure 11f**). Compound **44** was found to have stronger affinity (EBFE of -25.69 ± 3.39 kcal/mol) towards MbtA than

compound **49**. We also observed that the residues which are predominantly involved in binding ligands **44** and **49** are mostly situated at the C-terminal domain and at the end of the N-terminal domain. This indicates that ligands **44** and **49** may inhibit the movement of the C-terminal domain, which is crucial for MbtA mediated catalysis. In summary, the MD and MMPBSA analyses indicate that the binding between MbtA and ligands **44** and **49** is stable.

Table 5. Estimated binding free energies for MbtA-44 and MbtA-49 complexes

Complex	E_{vdW} (kcal/mol)	E_{elec} (kcal/mol)	G_{polar} (kcal/mol)	$G_{nonpolar}$ (kcal/mol)	EBFE (kcal/mol)
MbtA-44	-31.13±1.83	-11.93±2.10	21.05±2.22	-3.68±0.17	-25.69±3.39
MbtA-49	-25.01±2.76	-7.45±1.48	17.35±2.35	-3.00±0.24	-18.11±2.81

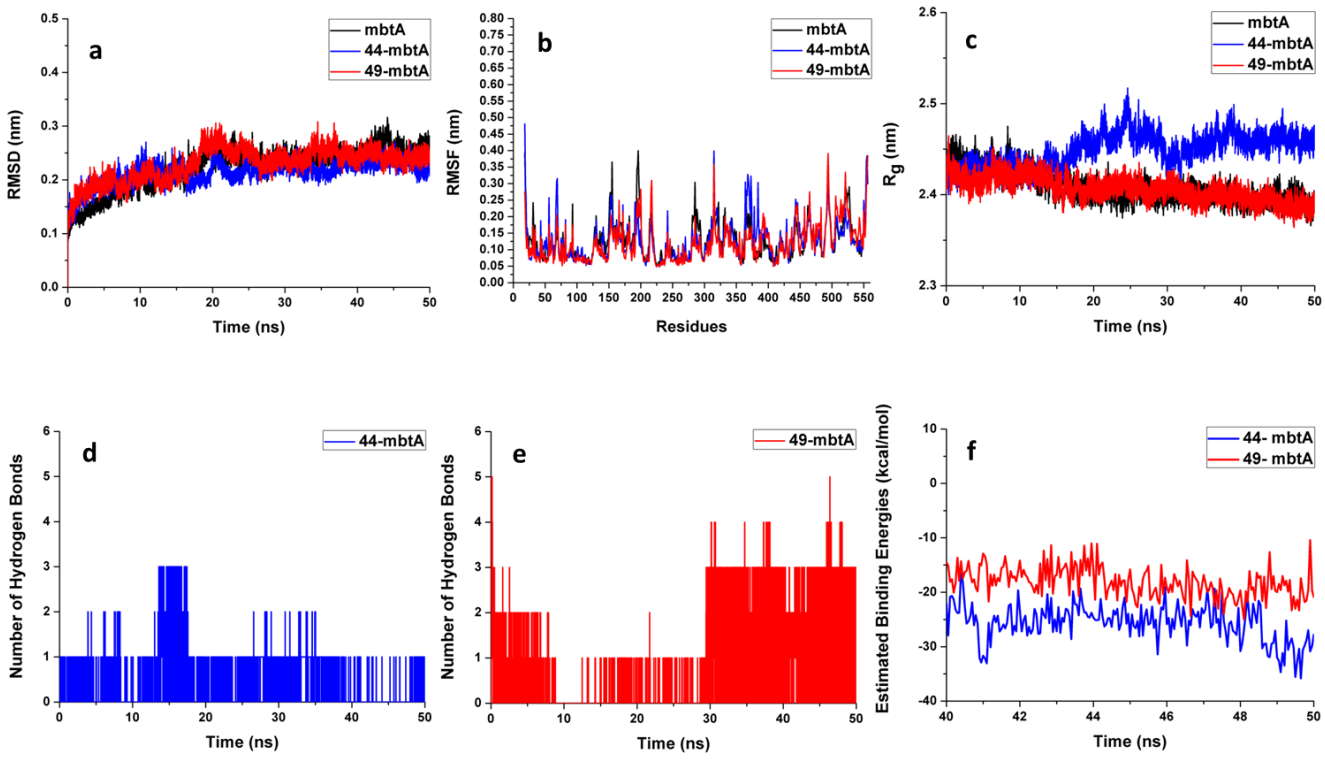

Figure 11. MD simulations and MMPBSA analyses indicate stable complexes between **44/49** and MbtA. **a.** RMSD analyses of simulations shows stability of the simulated complexes. **b.** Root mean square fluctuation (RMSF) analyses indicate higher mobility for N and C terminal residues **c.** Radius of gyration (R_g) analyses showed structural compactness of the systems remained stable after ~30 ns. **d.** and **e.** indicate the number of hydrogen bonds formed between

inhibitor and MbtA during the simulation and showed formation of stable complexes **f.** MMPBSA analyses of the MbtA-**44** and MbtA-**49** complexes indicate contribution of various non-covalent interactions that stabilize the protein-ligand complexes during simulation.

Effect of 44 and 49 on mycobacterial drug efflux pumps.

A distinctive feature of mycobacteria is their highly hydrophobic cell envelopes and prevalence of multidrug efflux pumps (EPs).[33] The role of EPs in microbes consists of expelling toxic metabolites from the bacterial cells and, most interestingly, these transmembrane proteins are very effective in preventing the intracellular accumulation of antimicrobial drugs.

Mycobacterial membrane protein large transporters (MmpL) are a subclass of efflux pumps found in mycobacteria.[34] In addition to the MmpL, accessory proteins MmpS4 and MmpS5 have been shown to interact with their cognate MmpL transporters to permit extrusion of NRPS-PKS gene metabolites. Most *mmpL* and *mmpS* genes are involved in the synthesis or modification of PKS and this close proximity suggests a possible role in the transport and/or biosynthesis of molecules synthesized by the neighbouring synthase gene products in mycobacteria species.[35]

In *M. smegmatis*, *mmpS4* is organized into an identical putative operon to the *mmpL4a* and *mmpL4b* gene clusters, which have been shown to be involved in biosynthesis of cell surface polyketide, glycopeptidolipids (GPL).[36] These surface polyketides are required for sliding motility and biofilm formation, and in some cases their level of production is correlated with strain virulence of NTM including in *M. abscessus* and *M. avium* pathogens.[37,38] On the other hand, targeted double deletion of the two iron-regulated *mmpS4* and *mmpS5* genes almost completely prevented secretion of carboxymycobactin and impaired growth of *M. tuberculosis* under iron-limiting conditions.[39] Studies indeed showed that both MmpS4 and MmpS5 can interact with MmpL5 to restore wild-type levels of siderophore and GPL secretion, while MmpL4 only interacts with MmpS4. Thus, the MmpL4/MmpS4, MmpL5/MmpS5 and MmpL5/MmpS4 complexes constitute inter-membrane siderophore exporters. Evidence suggested that disruption of MmpS4/MmpS5 activity might lead to self-poisoning of *M. tuberculosis* through the accumulation of active siderophores inside the cell.[40]

Based on their role in metabolite export, we hypothesized that a pocket for mycobactin binding should exist in MmpL4/MmpL5 complex (**Figure 12**, created with BioRender.com) in mycobacteria. We hypothesized that this pocket should have similar geometry to that of the mycobactin biosynthetic enzymes which accommodate the signature hydroxyphenyloxazoline moiety. As our compounds were designed based on the structure of the

hydroxyphenyloxazoline, we rationalized that these compounds should interfere with the MmpL4/MmpL5 complexes.

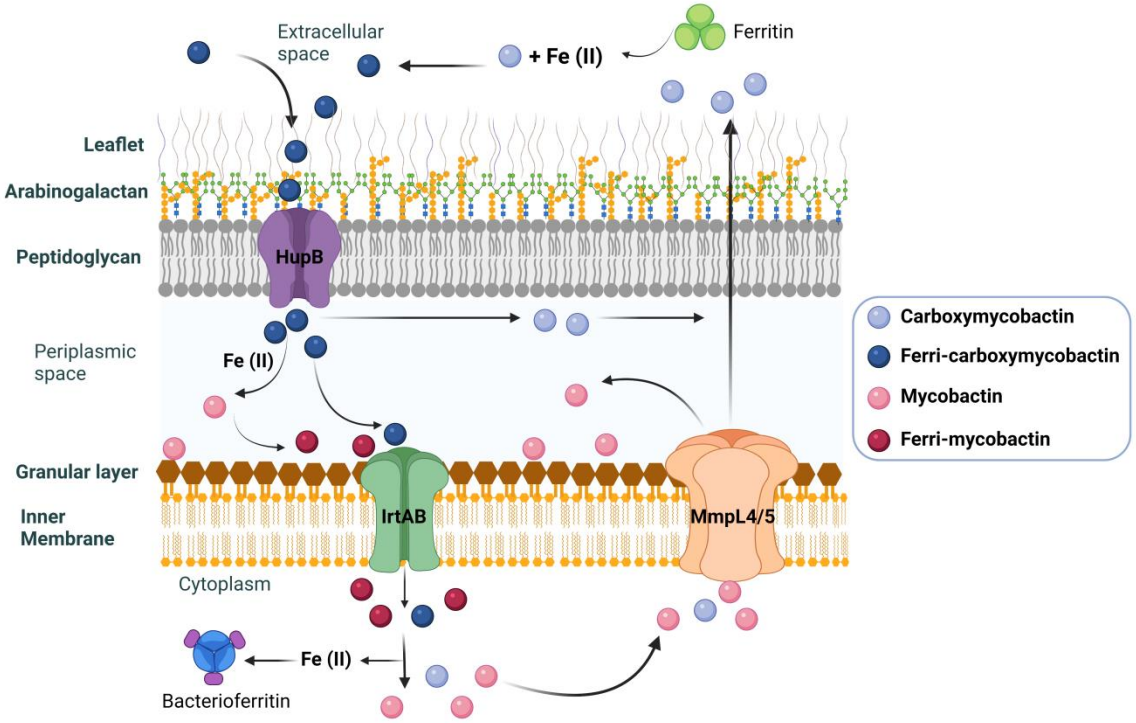

Figure 12. Transportation of hydrophilic Ferri-carboxymycobactin (Fe-cMBT) and lipophilic Ferri-mycobactin (Fe-MBT) complex through the complex lipidemic architecture. After releasing iron in the cytoplasmic space, cMBT and MBT are recycled *via* the MmpL4/5 efflux pump transporter.

Earlier research groups have used different non-virulent mycobacterial strains such as *M. smegmatis*,[41] *M. bovis* BCG[42] and *M. aurum*[43,44] as surrogate models to screen for novel EPIs to mitigate the emerging burden of efflux pump mediated drug-resistance in Mtb. We therefore tested compounds **44** and **49** in a whole-cell drug efflux pump inhibition assay using *M. smegmatis mc*^{2} *155* with ethidium bromide (EtBr) as the efflux substrate as a model for mycobacterial efflux pump inhibition. EtBr fluoresces when in complex with DNA, therefore if a tested compound is an efflux inhibitor, fluorescence will increase over time as EtBr accumulates inside the cell. Both **44** and **49** inhibited efflux pump activity more efficiently than known efflux pump inhibitors verapamil and chlorpromazine (**Figure 13**).

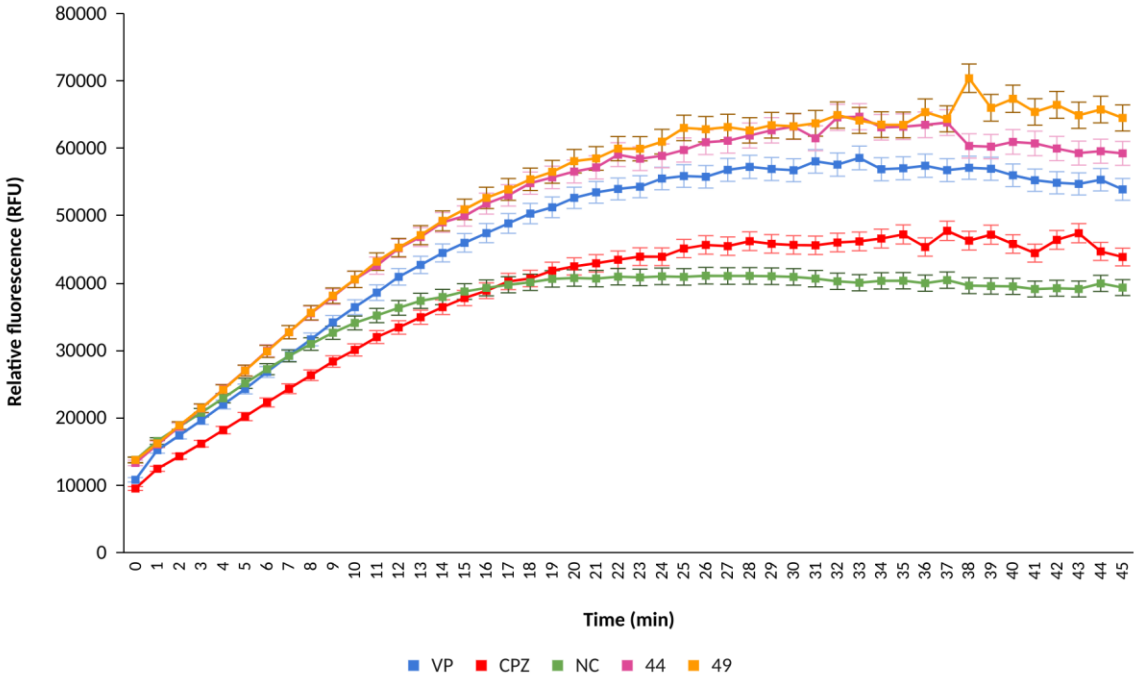

Figure 13. Accumulation of ethidium bromide (EtBr) within M. smegmatis cells in the presence of **44**, **49**, VP-verapamil, CPZ-chlorpromazine, NC-negative control (no inhibitor). Experiment was performed in biological triplicate (n=3), values represent the mean ±SD.

These primary findings in surrogate model bacteria[41] suggest that the third series of compounds may have pleiotropic modes of action, and the potential to reverse antimicrobial resistance in mycobacteria. However, further testing of the lead compounds against Mtb/DR-Mtb will be required to explore their potential against pathogens causing human infection and for tackling MDR/XDR-TB. Recently, Mtb acquired resistance towards bedaquiline was reported, caused by resistance-conferring mutations which increase expression of efflux pump proteins. This poses questions regarding the sustainability of the newer discoveries on the TB drug market[45] and there is a need for novel combinations of complementary drugs in TB treatment regimens. The off-target effects we have observed with compounds **44** and **49** (efflux inhibition in addition to MbtA inhibition) are of great interest in this regard, and have the potential to increase the effectiveness of existing TB drug treatment regimens which are prone to resistance caused by drug efflux. The potential of drug design efforts targeted towards efflux pump proteins is further highlighted by the discovery of SQ109, which targets MmpL3,[46] and furthermore research which indicated that increased transcription of *mmpS4-mmpS5* results in azole resistance[47] in Mtb mutant strains. Further studies to identify inhibitors against *mmpS4-*

mmpS5 could therefore be a possible mechanism to reverse this mechanism of drug resistance in mycobacteria by-way-of newer target based drug discovery.

Evaluation of Therapeutic Potential:

Cytotoxicity and therapeutic potential of compounds 44 and 49.

Compounds **44** and **49** were then subjected to cytotoxicity evaluation using RAW 264.7 and THP-1 cell lines following the REMA assay protocol.[44,48] The concentration (μg/mL) required for 90% growth inhibition (GIC_{90}) was determined and was used to calculate the selectivity index (SI). Both compounds exhibited selective toxicity towards *M. smegmatis, M. aurum, M. bovis* BCG, and *M. tuberculosis* (**Table 6**). The compounds showed cytotoxicity in a narrow range against RAW 264.7 and THP-1 cell lines and showed lower cytotoxicity potential compared to their antibacterial activity against *M. smegmatis*, *M. aurum*, and *M. bovis* BCG, and *M. tuberculosis*. The compounds exhibited equivalent cytotoxicity against both the cell lines and it could be inferred that different electron-withdrawing substitution at ring-C (phenyl ring) does not play any significant role in the cytotoxicity of **44** and **49**.

Table 6. Cytotoxicity evaluation of compounds **44** and **49** and Selectivity Index (SI) determination.

Code	Cell Line	GIC_{90} (μg/mL)	*M. smegmatis*		*M. aurum*		*M. bovis* BCG		*M. tuberculosis*	
			MIC_{90}	SI	MIC_{90}	SI	MIC_{90}	SI	MIC_{90}	SI
44	RAW 264.7	128	4	32	16	8	8	16	16	8
49		128	4	32	8	16	8	16	8	16
44	THP-1	64	4	16	16	4	8	16	16	4
49		64	4	16	8	8	8	16	8	8

*Growth inhibition assays are performed using the resazurin microtitre method.

Mycobacterial killing inside infected macrophages.

Mycobacteria are able to survive inside the host's primary immune cells under different stress conditions in either replicating, non-replicating or slowly-replicating states for an undefined period.[49] Considering the importance of target bacilli located within phagocytic cells to achieve host sterilization and absence of relapse, permeability of potential drug candidates within macrophages is a major requirement.[24] We therefore performed *in vivo* screening of the lead

compounds against intracellular surviving bacteria to mitigate the risk of hit failure in pre-clinical testing,[50] following our established spot culture growth inhibition (SPOTi) assay.[51] The slow growth and highly infectious nature of Mtb, combined with the requirement for sophisticated complex infrastructure for working with Mtb, pose major obstacles towards developing a comprehensive high-throughput, intracellular, drug screening procedure. To avoid the use of highly pathogenic, slow-growing Mtb in the early drug screening process, different mycobacterial species, such as *M. aurum*,[52] *M. abscessus*,[53] *M. marinum*,[54] *M. phlei*[53] and *M. bovis* BCG[55] have been utilized as surrogates over the years. Of these, the fast-growing non-pathogenic *M. aurum* possesses similar cell wall architecture to Mtb, moreover sharing gene organization, intracellular therapeutic targets and even drug resistance patterns. Additionally, mouse macrophage cell line RAW 264.7 has been considered as a suitable model for drug screening because of its high phagocytic activity, excellent adherence capability and ease of culturing.[56] The choice of this mouse macrophage is supported by the wide use of mice as an animal model for *in vivo* anti-TB drug testing.

We therefore evaluated compounds **44** and **49** in a macrophage infection model using *M. aurum* in the RAW 264.7 cell line using the SPOTi assay.[51] This *ex vivo* infection model mimics the host macrophage environment where intracellularly surviving mycobacteria are under iron-stress conditions.[24] Intracellular growth inhibition was monitored at 72 h for both candidates. The assay was performed in three biological replicates. In this whole-cell assay, **44** and **49**, each showed more than 90% growth inhibition at 16 μg/mL at 72 h (Supporting Information: Mycobacterial killing by **44** and **49** inside infected macrophages).

Drug-drug interaction evaluation.

A checkerboard assay was performed to test the activities of the lead candidates in combination with clinically approved first line TB drugs isoniazid (INH) and rifampicin (RIF) against *M. smegmatis mc*^{2} *155*.[48] Comparison of MICs of **44** and **49** alone and in combination with INH and RIF allowed fractional inhibitory concentrations (ΣFICs) to be calculated. In combination with INH, both **44** and **49** showed an additive profile (**Table 7**). The use of **44**/**49** with INH may therefore serve as an effective combination drug therapy for resistant TB, helping to eradicate antibacterial resistance associated with superbugs by targeting conditionally essential targets alongside pre-established essential targets. This mechanism of additivity has not been previously investigated.

Table 7. Antibiotic combination evaluation against *M. smegmatis* in checkerboard assay.

Drug-Combination	ΣFIC*	Activity
INH-44	0.6	Additive
INH-49	0.6	Additive
RIF-44	1.12	Indifference
RIF-49	1.12	Indifference

* Synergistic, FICI of ≤ 0.5; additive, FICI of >0.5 to ≤1; no interaction (indifference), FICI of >1 to ≤4; antagonistic, FICI of >4.

***In vivo* pharmacokinetic profiling of 44 and 49.**

A major challenge encountered in development of MbtA inhibitors over the years has been poor pharmacokinetic (PK) profile. Thus despite their excellent antitubercular profile, many inhibitors failed to entered the clinical pipeline. Compounds **44** and **49** were therefore subjected to *in vivo* PK profiling in dual cannulated male Sprague-Dawley rats following intravenous (IV, dose: 1 mg/kg) and oral (PO, dose: 5 mg/kg) administration (Supporting Information: *In vivo* pharmacokinetic study of **44** and **49**). PK parameters were calculated using the non-compartmental analysis (NCA) tool of the Phoenix® WinNonlin® 8.3 platform (**Table 8**).

Table 8. Mean pharmacokinetic parameters for compounds **44** and **49** following IV (dose: 1 mg/kg) and PO (dose: 5 mg/kg) administration to Sprague-Dawley rats.

Parameters	**44**		**49**	
	IV	PO	IV	PO
$C_{\circ}/C_{max}$	448 ± 186	51.6 ± 5.52	505 ± 75.4	47.4 ± 17.2
AUC_{last} (h*ng/mL)	190 ± 27.4	203 ± 19.3	155 ± 10.3	167 ± 38.2
AUC_{INF} (h*ng/mL)	197 ± 26.5	215 ± 25	167 ± 16.1	184 ± 28.2
$T_{1/2}$ (h)	4.76 ± 1.19	6.06 ± 1.04	5.42 ± 2.83	5.32 ± 0.341
T_{last} (h)	12	24	12	24 ± 6.93
V_{ss} (kg/L)	11.5 ± 3.28	NA	17.3 ± 7.95	NA
Cl (mL/min/kg)	84.8 ± 12.2	NA	100 ± 10	NA
%F	-	21	-	22

Area under curve (AUC), elimination half-life (T1/2), hepatic clearance (Cl), steady-state volume of distribution (Vss), oral bioavailability (%F).

Following a single IV bolus administration (1 mg/kg) of **44** or **49** to male Sprague-Dawley rats, mean plasma clearance was very high, 84.8 mL/min/kg and 100 mL/min/kg respectively,

approximately 1.5-fold to 1.8-fold higher than normal hepatic blood flow of rats. The mean volume of distribution was 11.5 L/kg for **44** and 17.3 L/kg for **49**, approximately 16-fold and 25-fold greater than 0.7 L/kg total body fluids respectively. This indicates higher distribution of the inhibitors in tissues. The median time to reach peak plasma concentration of **44** with a single peroral administration (5 mg/kg) was 0.25 h with C_{max} of 51.6 ng/mL and AUC_{last} (plasma exposure) of 203 ng*h/mL. Corresponding values for **49** were 0.25 h, 48.8 ng/mL and 167 ng*h/mL. The calculated oral bioavailabilities were found to be very similar for both compounds: 21% (**44**) and 22% (**49**).

In summary, these values show that both **44** and **49** display better peroral bioavailability and metabolic stability than previously reported MbtA inhibitor Sal-AMS[57] and all Sal-AMS analogues reported to date.[19] This is promising for further development of these inhibitors.

CONCLUSIONS

New antitubercular agents against novel targets are required to tackle tuberculosis due to emerging MDR, XDR and TDR mycobacterial strains. Key enzymes in the mycobactin biosynthetic pathway, such as MbtA and MbtB, are examples of novel targets for TB drug design. The goal of our research was to discover new lead compounds which target the conditionally essential mycobactin pathway of both non-pathogenic, fast growing and pathogenic, slow growing mycobacteria. To this end, we have rationally designed and synthesised three series of mycobactin inhibitors (49 compounds) mimicking the 2-hydroxyphenyloxazoline portion of mycobactin. Compounds were tested against both fast-growing non-pathogenic *M. smegmatis* and pathogenic *M. tuberculosis* in iron-rich (GAST-Fe medium) and iron-deprived (GAST medium) environments. The mycobactin biosynthesis pathway is commonly shared by both pathogenic and non-pathogenic strains of mycobacteria[12,13,19] and this approach was the rationale behind antimicrobial screening. Compounds in the first series bearing thiocarbamoyl substitution at the pyrazoline *N1* (**1**, **2**, **4** and **7**) were effective against *M. tuberculosis* under iron-deprived conditions, but did not show any effect against *M. smegmatis*. Compounds in the second series containing an acetyl group at *N1* position (**15**-**33**) were found to be inactive against both *M. smegmatis* and *M. tuberculosis*. Based on these results we propose that the target of **1**-**14** is MbtB, and that the presence of the *N1* thiocarbamoyl group is a requirement for interaction with the MbtB-Cy domain, although further experiments are required to verify this hypothesis. A putative MbtB target selectivity for these compounds is supported by the loss of activity observed on

replacement of thiocarbamoyl group with acetyl (**15-33**) or carbamoyl moieties. Compounds in the third series without any substitution at the *N1* position (**34**-**49**) were found to be active against both *M. smegmatis* and *M. tuberculosis*, with lead candidates **44** and **49** showing potent antitubercular activity. Candidates **44** and **49** showed clear target selectivity towards conditionally essential proteins in both *M. tuberculosis* and NTM, indicating their potential to counter opportunistic infections caused by NTM in immunocompromised patients. The mechanism of action of **44** and **49** appeared to be linked to the inhibition of siderophore production in mycobacteria. Results from thermofluorimetry assays and molecular dynamics simulations suggested that the antitubercular activity of **44** and **49** might stem from inhibition of MbtA. Based on the structural architecture of **44** and **49**, we propose that the pyrazoline ring acts as a mimic of salicylic acid, the native substrate of MbtA, thus inhibiting the conditionally essential mycobactin biosynthesis pathway. These findings expand our knowledge of the mechanisms of conditionally essential proteins and will support the rational design of new antitubercular compounds endowed with multitarget activity.

Different modes of action were observed for **44** and **49**, though both displayed growth inhibition in an *M. aurum* macrophage infection model and had favourable SI. Both candidates also showed additive effects with INH in *M. smegmatis* and had a favourable PK profile, highlighting their potential for use in antitubercular drug regimens. Additionally, we demonstrated that **44** and **49** can inhibit whole cell drug efflux pumps in *M. smegmatis*, highlighting their potential to reverse drug resistance in TB species which are resistant due to efflux mechanisms. We hope that this finding will instigate future research into pyrazoline analogues as MmpL inhibitors.

For the initial studies of **44** and **49** reported here, we selected to perform mechanism-of-action studies using *M. smegmatis* and *M. aurum* as model surrogates of Mtb, as it is known that the mycobactin biosynthesis pathway is shared by both pathogenic and non-pathogenic strains.[10,12,13,19] Verification of the mechanism-of-action of **44** and **49** in Mtb is therefore required, and future research in our lab will seek to confirm the mode of killing (by monitoring reduction in CFU count over time), efflux inhibition, mycobacterial killing inside macrophages and drug interactions of **44** and **49** in Mtb and DR-Mtb strains.

EXPERIMENTAL SECTION

Materials and Methods. All chemicals and solvents were of reagent grade, and were purchased from Sigma-Aldrich, Spectrochem, and Rankem. The completion of the reactions was monitored on commercially available pre-coated silica gel aluminium TLC plates (Merck)

visualized under UV light at 254 nm. Melting points were determined using the OptiMelt (Stanford Research Systems, Inc., USA) automated system apparatus. Intermediate chalcones were characterized by melting point. Final compounds were purified by re-crystallisation or by column chromatography on silica gel (60-120). Solvents are specified in the corresponding experiment. Lead compounds **44** and **49** showed 95% and greater than 95% purity in HPLC analysis. Final compounds were characterized by ^{1}H NMR and ^{13}C NMR spectra obtained from Bruker 300 or 500 MHz, or JEOL 400 MHz instruments. Deuterated dimethylsulfoxide, chloroform, and methanol (DMSO-d_6, $CDCl_3$, and CD_3OD) were used as solvents and tetramethylsilane taken as the internal standard. Chemical shifts (δ) were reported in parts per million (ppm). In ^{1}H NMR, the coupling constants are expressed in hertz (Hz). Splitting patterns are abbreviated as follows; singlet (s), doublet (d), triplet (t), quartet (q), multiplet (m), broard (br). Mass spectra were recorded using WATERS-QT of Premier-HAB213 using the (ESI-MS) Electrospray ionization technique. High resolution mass spectra (HRMS) were recorded on a Micromass Q-TOF Premier Tandem Mass Spectrometer coupled to CapLC using low-resolution ESI or high-resolution nano ESI techniques. The bacterial species used in the study were *M. smegmatis* mc^2 155 (ATCC 700084), *M. tuberculosis* H37Rv (ATCC 27294), *M. bovis* BCG and *M. aurum* (ATCC 10437). The cell lines utilized for cytotoxicity studies were the human peripheral blood monocyte derived cell line THP-1 and murine macrophage cell line RAW 264.7. Mycobacterial species were cultured in glycerol-alanine-salts (GAST) medium and iron-supplemented glycerol-alanine-salts (GAST-Fe) medium. Checkerboard assays used GAST agar supplemented with oleic acid-albumin-dextrose-catalase (OADC) enrichment purchased from BD biosciences. All reagents were purchased from Sigma-Aldrich unless stated otherwise. Readings were taken in SpectraMax M3 instrument (Molecular Devices), and BioTek Synergy2 (Gen5) instruments. Biological data was statistically treated using ANOVA (GraphPad Prism, Version 8).

Chemistry

General procedure for the synthesis of 2'-hydroxybenzylidene acetophenones (chalcones, C1-C19)

To a solution of *o*-hydroxyacetophenone (0.01 M) and the appropriate aromatic aldehyde (0.01 M), an aqueous solution of sodium hydroxide (60% w/v, 15 mL) was added drop-wise over a period of 2 h on ice with continuous stirring. The reaction mixture was then stirred for 48 h at room temperature. The resulting thick reddish slurry was acidified (pH adjusted to 2) using ice-cooled hydrochloric acid (6 N) resulting in a yellow precipitate which was recrystallized from ethanol.

General procedure for synthesis of 3,5-diaryl-4,5-dihydro*1H*-pyrazole-1-carbothioamides (1-14)

To a solution of the appropriate chalcone (0.5 mM) and thiosemicarbazide (1.39 mM) in methanol (20 mL), was added potassium hydroxide (0.025 M, 5 mL) and the mixture was refluxed for a period of 8-10 h. The solution was then diluted with 50 mL ice-cooled water and subsequently the pH was adjusted to 2 with ice-cooled hydrochloric acid (6 N). The resulting white precipitate was filtered, washed with water and dried. The precipitate was further purified by column chromatography using petroleum ether and ethyl acetate (8:2).

***3-(2-hydroxyphenyl)-5-(4-hydroxyphenyl)-4,5-dihydro-1H-pyrazol-1-carbothioamide* (1)**

White amorphous powder; yield 51%; mp (°C) 207-209; ^{1}H-NMR (400 MHz, DMSO-d_6) δ (ppm) 3.193 (d, *J=1.6 Hz*, 1H), 3.878 (dd, J_{AM}*=18.4 Hz*, J_{AM}*=5.8 Hz*, 1H), 5.766 (dd, J_{MA}*=10.8 Hz*, J_{MX}*=1.4 Hz*, 1H), 6.652-7.584 (m, Ar-H, 8H), 7.969 (s(br), -C(=S)-NH_2, 2H), 9.293 & 9.707 (2s , 2Ar-OH, 2H); ^{13}C-NMR (400 MHz, DMSO-d_6) δ (ppm) 44.59, 61.92, 115.65, 116.61, 117.36, 120.06, 127.13, 130.11, 132.57, 133.76, 156.86, 156.98, 157.07; HRMS (m/z) calcd. for $C_{16}H_{15}N_3O_2S$ $(M+H)^+$ 314.0963, found 314.0957.

***3-(2-hydroxyphenyl)-5-phenyl-4,5-dihydro-1H-pyrazol-1-carbothioamide* (2)**

White amorphous powder; yield: 55%; mp (°C): 177-178; ^{1}H-NMR (400 MHz, DMSO-d_6) δ (ppm) 3.205 (d, J_{AM}*=7.8 Hz*, H_A), 3.959 (dd, J_{MA}*=18.0 Hz*, J_{MX}*=5.6 Hz*, H_M), 5.893 (d, J_{MX}*=4.6 Hz*, H_X), 6.847-7.634 (m, Ar-H, 9H), 8.050 (s(br), -C(=S)-NH_2, 2H), 9.715 (s, Ar-OH, 1H); ^{13}C-NMR (125 MHz, $CDCl_3$) δ (ppm) 43.62, 62.41, 114.77, 117.36, 120.33, 125.55, 128.09, 129.20, 129.21, 133.31, 141.23, 157.76, 158.96, 176.43; HRMS (m/z) calcd. for $C_{16}H_{15}N_3OS$ $(M+H)^+$ 298.1014, found 298.1012.

***3,5-bis(2-hydroxyphenyl)-4,5-dihydro-1H-pyrazol-1-carbothioamide* (3)**

White amorphous powder; yield: 56%; mp (°C): 212-215; ^{1}H-NMR (400 MHz, DMSO-d_6) δ (ppm) 3.073 (dd, J_{AM}*=17.6 Hz*, J_{AX}*=1.4 Hz*, H_A), 3.864 (dd, J_{MA}*=18.0 Hz*, J_{MX}*=5.8 Hz*, H_M), 5.964 (dd, J_{MX}*=11.2 Hz*, J_{AX}*=1.0 Hz*, H_X), 6.709-6.904 (m, Ar-H, 8H), 8.012 (s(br), -C(=S)-NH_2, 2H), 9.702 & 9.614 (2s, 2Ar-OH, 2H); ^{13}C-NMR (400 MHz, DMSO-d_6) δ (ppm) 44.65, 62.32, 112.27, 114.45, 116.39, 117.38, 120.09, 130.11, 132.64, 145.15, 156.88, 157.06, 158.01, 176.24; HRMS (m/z) calcd. for $C_{16}H_{15}N_3O_2S$ $(M+H)^+$ 314.0963, found 314.0958.

***3-(2-hydroxyphenyl)-5-(3-hydroxyphenyl)-4,5-dihydro-1H-pyrazol-1-carbothioamide* (4)**

White amorphous powder; yield: 49%; mp (°C): 211-213; ^{1}H-NMR (400 MHz, DMSO-d_6) δ (ppm) 3.158 (dd, J_{AM}*=18.2 Hz*, J_{AX}*=1.6 Hz*, H_A), 3.901 (dd, J_{MA}*=18.0 Hz*, J_{MX}*=5.8 Hz*, H_M), 5.782 (dd, J_{MX}*=11.6 Hz*, J_{AX}*=1.4 Hz*, H_X), 6.464-7.058 (m, Ar-H, 8H), 8.032 (s(br), -C(=S)-NH_2, 2H), 9.346 & 9.704 (2s, 2Ar-OH, 2H); ^{13}C-NMR (125 MHz, CD_3OD) δ (ppm) 44.95,

63.73, 113.08, 115.36, 116.82, 117.56, 117.88, 120.91, 130.57, 130.92, 133.59, 145.37, 158.69, 158.94, 159.78, 177.72; HRMS (m/z) calcd. for $C_{16}H_{15}N_3O_2S$ $(M+H)^+$ 314.0963, found 314.0966.

3-(2-hydroxyphenyl)-5-(o-tolyl)-4,5-dihydro-1H-pyrazol-1-carbothioamide **(5)**

White amorphous powder; yield: 57%; mp (°C): 181-183; ^{1}H-NMR (400 MHz, DMSO-d_6) δ (ppm) 2.357 (s, Ar-CH_3, 3H), 3.061 (dd, J_{AM}*=18.0 Hz*, J_{AX}*=1.6 Hz*, H_A), 3.999 (dd, J_{MA}*=18.0 Hz*, J_{MX}*=5.8 Hz*, H_M), 5.969 (d, J_{MX}*=4.2 Hz*, H_X), 6.765-7.605 (m, Ar-H, 8H), 8.078 (s(br), -C(=S)-NH_2, 2H), 9.692 (s, Ar-OH, 1H); ^{13}C-NMR (125 MHz, $CDCl_3$) δ (ppm) 19.71, 42.66, 59.73, 114.84, 117.34, 120.29, 123.66, 126.98, 127.91, 129.17, 131.06, 133.27, 133.82, 139.42, 157.73, 158.94, 176.25; HRMS (m/z) calcd. for $C_{17}H_{17}N_3OS$ $(M+H)^+$ 312.1171, found 312.1166.

3-(2-hydroxyphenyl)-5-(p-tolyl)-4,5-dihydro-1H-pyrazol-1-carbothioamide **(6)**

White amorphous powder; yield: 63%; mp (°C): 201-204; ^{1}H-NMR (400 MHz, DMSO-d_6) δ (ppm) 2.230 (s, Ar-CH_3, 3H), 3.182 (dd, J_{AM}*=18.2 Hz*, J_{AX}*=1.8 Hz*, H_A), 3.930 (dd, J_{MA}*=18.4 Hz*, J_{MX}*=5.8 Hz*, H_M), 5.847 (dd, J_{MX}*=11.2 Hz*, J_{AX}*=1.4 Hz*, H_X), 6.850-7.624 (m, Ar-H, 8H), 8.023 (s(br), C(=S)-NH_2, 2H), 9.710 (s, Ar-OH, 1H); ^{13}C-NMR (125 MHz, $CDCl_3$) δ (ppm) 21.30, 43.65, 62.22, 115.14, 117.34, 120.31, 125.49, 129.21, 129.85, 133.26, 141.74, 150.94, 157.75, 161.32, 176.36; HRMS (m/z) calcd. for $C_{17}H_{17}N_3OS$ $(M+H)^+$ 312.1171, found 312.1174.

3-(2-hydroxyphenyl)-5-(2-methoxyphenyl)-4,5-dihydro-1H-pyrazol-1-carbothioamide **(7)**

White amorphous powder; yield: 55%; mp (°C): 197-199; ^{1}H-NMR (400 MHz, DMSO-d_6) δ (ppm) 3.057 (dd, J_{AM}*=18.0 Hz*, J_{AX}*=1.6 Hz*, H_A), 3.801 (s, Ar-OCH_3, 3H), 3.897 (dd, J_{MA}*=18.2 Hz*, J_{MX}*=5.6 Hz*, H_M), 6.024 (d, J_{MX}*=4.4Hz*, H_X), 6.772-7.591(m, Ar-H, 8H), 8.055 (s(br), -C(=S)-NH_2, 2H), 9.688 (s, Ar-OH, 1H); ^{13}C-NMR (400 MHz, DMSO-d_6) δ (ppm) 44.63, 55.50, 62.33, 111.80, 112.28, 116.74, 117.38, 117.66, 120.05, 130.10, 130.27, 132.63, 145.02, 156.84, 157.07, 159.87, 176.37; HRMS (m/z) calcd. for $C_{17}H_{17}N_3O_2S$ $(M+H)^+$ 328.1120, found 328.1124.

3-(2-hydroxyphenyl)-5-(3-methoxyphenyl)-4,5-dihydro-1H-pyrazol-1-carbothioamide **(8)**

White amorphous powder; yield: 49%; mp (°C): 127-129; ^{1}H-NMR (400 MHz, DMSO-d_6) δ (ppm) 3.201 (dd, J_{AM}*=18.2 Hz*, J_{AX}*=1.2 Hz*, H_A), 3.692 (s, Ar-OCH_3, 3H), 3.934 (dd, J_{MA}*=18.2Hz*, J_{MX}*=5.8 Hz*, H_M), 5.866 (d, J_{MX}*=4.4 Hz*, H_X), 6.652-7.625 (m, Ar-H, 8H), 8.053 (s(br), -C(=S)-NH_2, 2H), 9.712 (s, Ar-OH, 1H); ^{13}C-NMR (400 MHz, DMSO-d_6) δ (ppm) 43.40, 55.96, 58.37, 111.82, 116.65, 117.21, 119.91, 120.55, 125.61, 128.63, 130.10, 130.40,

132.56, 156.11, 157.00, 157.51, 176.21; HRMS (m/z) calcd. for $C_{17}H_{17}N_3O_2S$ $(M+H)^+$ 328.1120, found 328.1114.

3-(2-hydroxyphenyl)-5-(4-methoxyphenyl)-4,5-dihydro-1H-pyrazol-1-carbothioamide **(9)**

White amorphous powder; yield: 58%; mp (°C): 187-188; ^{1}H-NMR (400 MHz, DMSO- d_6) δ (ppm) 3.199 (dd, J_{AM}*=18.2 Hz*, J_{AX}*=1.2 Hz*, H_A), 3.688 (s, Ar-OCH_3, 3H), 3.918 (dd, J_{MA}*=18.6 Hz*, J_{MX}*=5.6 Hz*, H_M), 5.833 (dd, J_{MX}*=11.0 Hz*, J_{AX}*=1.2 Hz*, H_X), 6.832-7.625 (m, Ar-H, 8H), 8.006 (s(br), -C(=S)-NH_2, 2H), 9.716 (s, Ar-OH, 1H); ^{13}C-NMR (400 MHz, DMSO-d_6) δ (ppm) 44.62, 55.56, 61.87, 114.36, 116.67, 117.37, 120.06, 127.12, 130.02, 132.60, 135.48, 156.90, 157.07, 158.73, 176.26; HRMS (m/z) calcd. for $C_{17}H_{17}N_3O_2S$ $(M+H)^+$ 328.1120, found 328.1109.

5-(3-hydroxy-4-methoxyphenyl)-3-(2-hydroxyphenyl)-4,5-dihydro-1H-pyrazole-1-carbothioamide **(10)**

White amorphous powder; yield: 53%; mp (°C): 234-237; ^{1}H-NMR (400 MHz, DMSO-d_6) δ (ppm) 3.173 (dd, J_{AM}*=18.0 Hz*, J_{AX}*=1.6 Hz*, H_A), 3.690 (s, Ar-OCH_3, 3H), 3.886 (dd, J_{MA}*=18.4 Hz*, J_{MX}*=5.8 Hz*, H_M), 5.745 (dd, J_{MX}*=11.2 Hz*, J_{AX}*=1.2 Hz*, H_X), 6.513-7.955 (m, Ar-H, 7H), 8.492 (s(br), C(=S)-NH_2, 2H), 9.029 & 9.716 (2s, 2Ar-OH, 2H); ^{13}C-NMR (125 MHz, CD_3OD) δ (ppm) 44.97, 56.45, 63.43, 112.95, 113.49, 116.83, 117.87, 117.95, 120.91, 130.58, 133.57, 136.76, 147.86, 148.42, 158.70, 159.86, 177.65; HRMS (m/z) calcd. for $C_{17}H_{17}N_3O_3S$ $(M+H)^+$ 344.1069, found 344.1065.

5-(2-chlorophenyl)-3-(2-hydroxyphenyl)-4,5-dihydro-1H-pyrazol-1-carbothioamide **(11)**

White amorphous powder; yield: 49%; mp (°C): 243-244; ^{1}H-NMR (400 MHz, DMSO-d_6) δ (ppm) 3.136 (dd, J_{AM}*=18.2 Hz*, J_{AX}*=1.8 Hz*, H_A), 4.048 (dd, J_{MA}*=18.2 Hz*, J_{MX}*=5.8 Hz*, H_M), 6.106 (dd, J_{MX}*=12.0 Hz*, J_{AX}*=1.8 Hz*, H_X), 6.839-7.656 (m, Ar-H, 8H), 8.166 (s(br), -C(=S)-NH_2, 2H), 9.704 (s,ArOH, 1H); ^{13}C-NMR (125 MHz, $CDCl_3$) δ (ppm) 42.56, 60.36, 114.66, 117.35, 120.35, 126.01, 127.50, 129.23, 129.26, 130.32, 131.47, 133.40, 138.11, 157.72, 159.30, 176.50; HRMS (m/z) calcd. for $C_{16}H_{14}ClN_3OS$ $(M+H)^+$ 332.0624, found 332.0622.

5-(3-chlorophenyl)-3-(2-hydroxyphenyl)-4,5-dihydro-1H-pyrazol-1-carbothioamide **(12)**

White amorphous powder; yield: 41%; mp (°C): 254-255; ^{1}H-NMR (400 MHz, DMSO-d_6) δ (ppm) 3.239 (dd, J_{AM}*=18.4 Hz*, J_{AX}*=1.6 Hz*, H_A), 3.958 (dd, J_{MA}*=18.2 Hz*, J_{MX}*=5.8 Hz*, H_M), 5.894 (d, J_{MX}*=4.0 Hz*, H_X), 6.852-7.645 (m, Ar-H, 8H), 8.117 (s(br), -C(=S)-NH_2, 2H), 9.712 (s,ArOH, 1H); ^{13}C-NMR (125 MHz, $CDCl_3$) δ (ppm) 42.54, 60.36, 114.66, 117.34, 120.35, 126.01, 127.50, 129.23, 129.26, 130.32, 131.47, 133.40, 138.11, 157.71, 159.30, 176.50; HRMS (m/z) calcd. for $C_{16}H_{14}ClN_3OS$ $(M+H)^+$ 332.0624, found 332.0626.

5-(4-chlorophenyl)-3-(2-hydroxyphenyl)-4,5-dihydro-1H-pyrazol-1-carbothioamide **(13)**

White amorphous powder; yield: 59%; mp (°C): 221-223; ^{1}H-NMR (400 MHz, DMSO-d_6) δ (ppm) 3.210 (d, J_{AM}=*9.0 Hz*, H_A), 3.951 (dd, J_{MA}=*17.8 Hz*, J_{MX}=*6.0 Hz*, H_M), 5.871 (d, J_{MX}=*5.2 Hz*, H_X), 6.862-7.634 (m, Ar-H, 8H), 8.080 (s(br), -C(=S)-NH_2, 2H), 9.721 (s,Ar-OH, 1H); ^{13}C-NMR (125 MHz, $CDCl_3$) δ (ppm) 43.49, 61.81, 114.61, 117.43, 120.41, 127.13, 129.17, 129.38, 133.46, 133.90, 139.78, 157.75, 158.79, 176.41; HRMS (m/z) calcd. for $C_{16}H_{14}ClN_3OS$ $(M+H)^+$ 332.0624, found 332.0624.

5-(2-fluorophenyl)-3-(2-hydroxyphenyl)-4,5-dihydro-1H-pyrazol-1-carbothioamide **(14)**

Off-white amorphous powder; yield: 48%; mp (°C): 201-204; ^{1}H-NMR (400 MHz, DMSO-d_6) δ (ppm) 3.228 (dd, J_{AM}=*18.2 Hz*, J_{AX}=*1.6 Hz*, H_A), 4.007 (dd, J_{MA}=*18.0 Hz*, J_{MX}=*5.8 Hz*, H_M), 6.021 (dd, J_{MX}=*11.8 Hz*, J_{AX}=*1.8 Hz*, H_X), 6.813-7.600(m, Ar-H, 8H), 8.091 (s(br), -C(=S)-NH_2, 2H), 9.755 (s,Ar-OH, 1H); ^{13}C-NMR (400 MHz, DMSO-d_6) δ (ppm) 43.58, 57.14, 116.14, 116.53, 117.40, 120.13, 124.96, 127.67, 129.22, 129.58, 130.13, 132.74, 156.90, 157.06, 176.20; HRMS (m/z) calcd. for $C_{16}H_{14}FN_3OS$ $(M+H)^+$ 316.0920, found 332.0918.

General procedure for synthesis of 1-(3,5-diaryl-4,5-dihydro1H-pyrazol-1-yl)ethan-1-ones (15-33)

A solution of the appropriate chalcone (0.10 mM) and excess hydrazine hydrate (0.13 mM) in glacial acetic acid (8 mL) was refluxed for 6 h. The reaction mixture was then poured into 100 g crushed ice. The resulting white precipitate was then filtered, washed with water and dried. The product was recrystallized from ethanol.

1-(3-(2-hydroxyphenyl)-5-phenyl-4,5-dihydro-1H-pyrazol-1-yl) ethan-1-one **(15)**

White amorphous powder; yield: 81%; mp (°C): 132-133; ^{1}H-NMR (400 MHz, DMSO-d_6) δ (ppm) 2.293 (s, -C(=O)-CH_3, 3H) 3.256 (d, J_{AM}=*11.6 Hz*, J_{AX}=*2.2 Hz*, H_A), 3.963 (dd, J_{MA}=*18.2 Hz*, J_{MX}=*6.0 Hz*, H_M), 5.509 (dd, J_{MX}=*11.6 Hz*, J_{AX}=*2.0 Hz*, H_X), 6.903-7.577 (m, ArH, 9H), 8.091 (s(br), -C(=S)-NH_2, 2H), 10.189 (s,Ar-OH, H); ^{13}C-NMR (400 MHz, DMSO-d_6) δ (ppm) 22.39, 44.28, 59.01, 117.08, 120.17, 126.03, 127.84, 129.27, 132.46, 142.81, 156.26, 157.32, 167.62; HRMS (m/z) calcd. for $C_{17}H_{16}N_2O_2$ $(M+H)^+$ 281.1290, found 281.1288.

1-(3,5-bis(2-hydroxyphenyl)-4,5-dihydro-1H-pyrazol-1-yl) ethan-1-one **(16)**

White amorphous powder; yield: 81%; mp (°C): 230-232 (Lit. 238-240); ^{1}H-NMR (400 MHz, DMSO-d_6) δ (ppm) 2.301 (s, -C(=O)-CH_3, 3H) 3.148 (dd, J_{AM}=*18.2 Hz*, J_{AX}=*2.4 Hz*, H_A), 3.889 (dd, J_{MA}=*18.0 Hz*, J_{MX}=*6.0 Hz*, H_M), 5.589 (dd, J_{MX}=*11.8 Hz*, J_{AX}=*2.2 Hz*, H_X), 6.699-7.542 (m, Ar-H, 8H), 9.665 & 10.250 (2s, 2Ar-OH, 2H); ^{13}C-NMR (400 MHz, DMSO-d_6) δ (ppm) 22.35, 42.85, 55.19, 116.01, 116.77, 116.99, 119.39, 120.14, 126.54, 128.01, 128.74, 129.58,

132.31, 154.59, 156.98, 157.30, 167.40; HRMS (m/z) calcd. for $C_{17}H_{16}N_2O_3$ $(M+H)^+$ 297.1239, found 297.1233.

1-(3-(2-hydroxyphenyl)-5-(3-hydroxyphenyl)-4,5-dihydro-1H-pyrazol-1-yl) ethan1-one **(17)**

White amorphous powder; yield: 77%; mp (°C): 183-185; ^{1}H-NMR (400 MHz, DMSO-d_6) δ (ppm) 2.264 (s, -C(=O)-CH_3, 3H) 3.207 (dd, J_{AM}*=18.2 Hz*, J_{AX}*=2.2 Hz*, H_A), 3.894 (dd, J_{MA}*=18.6 Hz*, J_{MX}*=5.8 Hz*, H_M), 5.388 (dd, J_{MX}*=12.0 Hz*, J_{AX}*=2.2 Hz*, H_X), 6.545-7.557 (m, Ar-H, 8H), 9.377 & 10.182 (2s, 2Ar-OH, 2H); ^{13}C-NMR (400 MHz, DMSO-d_6) δ (ppm) 22.35, 42.85, 55.19, 116.01, 116.77, 116.99, 119.39, 120.14, 126.54, 128.01, 128.74, 129.58, 132.31, 154.59, 156.98, 157.30, 167.40; HRMS (m/z) calcd. for $C_{17}H_{16}N_2O_3$ $(M+H)^+$ 297.1239, found 297.1233.

1-(3-(2-hydroxyphenyl)-5-(4-hydroxyphenyl)-4,5-dihydro-1H-pyrazol-1-yl) ethan1-one **(18)**

White amorphous powder; yield: 85%; mp (°C): 245-246 (Lit. 240-242); ^{1}H-NMR (400 MHz, DMSO-d_6) δ (ppm) 2.200 (s, -C(=O)-CH_3, 3H) 3.231 (dd, J_{AM}*=18.2 Hz*, J_{AX}*=2.0 Hz*, H_A), 3.896 (dd, J_{MA}*=18.2 Hz*, J_{MX}*=6.0 Hz*, H_M), 5.403 (dd, J_{MX}*=11.4 Hz*, J_{AX}*=2.2 Hz*, H_X), 6.686-7.564 (m, Ar-H, 8H), 9.350 & 10.200 (2s, 2Ar-OH, 2H); ^{13}C-NMR (400 MHz, DMSO-d_6) δ (ppm) 22.43, 43.95, 58.52, 115.83, 116.95, 120.16, 127.35, 129.64, 132.38, 133.12, 156.39, 157.14, 157.30, 167.42; HRMS (m/z) calcd. for $C_{17}H_{16}N_2O_3$ $(M+H)^+$ 297.1239, found 297.1237.

1-(3-(2-hydroxyphenyl)-5-(o-tolyl)-4,5-dihydro-1H-pyrazol-1-yl) ethan-1-one **(19)**

White amorphous powder; yield: 74%; mp (°C): 155-156; ^{1}H-NMR (400 MHz, DMSO-d_6) δ (ppm) 2.322 (s, Ar-CH_3, 3H) 2.379 (s, -C(=O)-CH_3, 3H) 3.129 (dd, J_{AM}*=18.4 Hz*, J_{AX}*=2.4 Hz*, H_A), 4.015 (dd, J_{MA}*=18.2 Hz*, J_{MX}*=5.8 Hz*, H_M), 5.620 (dd, J_{MX}*=12.0 Hz*, J_{AX}*=2.4 Hz*, H_X), 6.897-7.561 (m, Ar-H, 8H), 10.194 (s,Ar-OH, H); ^{13}C-NMR (400 MHz, DMSO-d_6) δ (ppm) 19.56, 22.35, 43.35, 56.37, 116.86, 120.16, 124.39, 126.88, 127.60, 129.53, 131.06, 132.45, 134.58, 140.62, 156.42, 157.30, 167.50; HRMS (m/z) calcd. for $C_{18}H_{18}N_2O_2$ $(M+H)^+$ 295.1447, found 297.1453.

1-(3-(2-hydroxyphenyl)-5-(p-tolyl)-4,5-dihydro-1H-pyrazol-1-yl) ethan-1-one **(20)**

White amorphous powder; yield: 79%; mp (°C): 131-134; ^{1}H-NMR (400 MHz, DMSO-d_6) δ (ppm) 2.263 (s, Ar-CH_3, 3H) 2.277 (s, -C(=O)-CH_3, 3H) 3.233 (dd, J_{AM}*=18.4 Hz*, J_{AX}*=2.2 Hz*, H_A), 3.934 (dd, J_{MA}*=18.2 Hz*, J_{MX}*=5.8 Hz*, H_M), 5.463 (dd, J_{MX}*=11.6 Hz*, J_{AX}*=2.2 Hz*, H_X), 6.903-7.566 (m, Ar-H, 8H), 10.189 (s,Ar-OH, H); ^{13}C-NMR (400 MHz, DMSO-d_6) δ (ppm) 21.20, 22.38, 44.17, 58.76, 117.05, 120.15, 125.99, 129.74, 132.40, 136.97, 139.85, 156.26, 157.30, 167.49; HRMS (m/z) calcd. for $C_{18}H_{18}N_2O_2$ $(M+H)^+$ 295.1447, found 297.1450.

1-(3-(2-hydroxyphenyl)-5-(2-methoxyphenyl)-4,5-dihydro-1H-pyrazol-1-yl) ethan1-one **(21)**

White amorphous powder; yield: 72%; mp (°C): 181-183; ^{1}H-NMR (400 MHz, DMSO-d_6) δ (ppm) 2.311 (s, -C(=O)-CH_3, 3H) 3.102 (dd, J_{AM}=*18.4 Hz*, J_{AX}=*2.2 Hz*, H_A), 3.812 (s, Ar-OCH_3, 3H) 3.903 (dd, J_{MA}=*18.2 Hz*, J_{MX}=*6.0 Hz*, H_M), 5.624 (dd, J_{MX}=*11.8 Hz*, J_{AX}=*2.2 Hz*, H_X), 6.857-7.539 (m, Ar-H, 8H), 10.217 (s,Ar-OH, H); ^{13}C-NMR (400 MHz, DMSO-d_6) δ (ppm) 22.34, 43.09, 54.85, 56.11, 111.90, 116.88, 120.13, 120.86, 126.01, 129.32, 132.35, 156.37, 156.79, 157.26, 167.43; HRMS (m/z) calcd. for $C_{18}H_{18}N_2O_3$ $(M+H)^+$ 311.1396, found 311.1399.

***1-(3-(2-hydroxyphenyl)-5-(3-methoxyphenyl)-4,5-dihydro-1H-pyrazol-1-yl) ethan1-one* (22)**

White amorphous powder; yield: 69%; mp (°C): 175-177; ^{1}H-NMR (400 MHz, DMSO-d_6) δ (ppm) 2.297 (s, -C(=O)-CH_3, 3H) 3.247 (dd, J_{AM}=18.4 Hz, J_{AX}=2.2 Hz, H_A), 3.731 (s, Ar-OCH_3, 3H) 3.938 (dd, J_{MA}=18.2 Hz, J_{MX}=6.0 Hz, H_M), 5.478 (dd, J_{MX}=11.6 Hz, J_{AX}=2.2 Hz, H_X), 6.752-7.569 (m, Ar-H, 8H), 10.181 (s, Ar-OH, H); ^{13}C-NMR (400 MHz, DMSO-d_6) δ (ppm) 22.36, 44.23, 55.48, 58.93, 111.79, 112.91, 116.81, 117.84, 120.14, 129.62, 130.27, 132.27, 144.49, 156.25, 157.29, 160.03, 167.61; HRMS (m/z) calcd. for $C_{18}H_{18}N_2O_3$ $(M+H)^+$ 311.1396, found 311.1397.

***1-(3-(2-hydroxyphenyl)-5-(4-methoxyphenyl)-4,5-dihydro-1H-pyrazol-1-yl) ethan1-one* (23)**

White amorphous powder; yield: 75%; mp (°C): 147-149; ^{1}H-NMR (400 MHz, DMSO-d_6) δ (ppm) 2.269 (s, -C(=O)-CH_3, 3H) 3.249 (dd, J_{AM}=*18.4 Hz*, J_{AX}=*2.2 Hz*, H_A), 3.720 (s, Ar-OCH_3, 3H) 3.920 (dd, J_{MA}=*18.2 Hz*, J_{MX}=*6.0 Hz*, H_M), 5.455 (dd, J_{MX}=*11.6 Hz*, J_{AX}=*2.2 Hz*, H_X), 6.867-7.570 (m, Ar-H, 8H), 10.195 (s,Ar-OH, H); ^{13}C-NMR (400 MHz, DMSO-d_6) δ (ppm) 22.40, 44.10, 55.64, 58.47, 114.54, 117.04, 120.15, 127.28, 129.62, 132.39, 134.81, 156.31, 157.30, 159.00, 167.47; HRMS (m/z) calcd. for $C_{18}H_{18}N_2O_3$ $(M+H)^+$ 311.1396, found 311.1392.

***1-(5-(3-hydroxy-4-methoxyphenyl)-3-(2-hydroxyphenyl)-4,5-dihydro-1H-pyrazol-1yl) ethan-1-one* (24)**

White amorphous powder; yield: 83%; mp (°C): 147-148; ^{1}H-NMR (400 MHz, DMSO-d_6) δ (ppm) 2.268 (s, -C(=O)-CH_3, 3H) 3.231 (dd, J_{AM}=*18.4 Hz*, J_{AX}=*1.8 Hz*, H_A), 3.721 (s, Ar-OCH_3, 3H) 3.888 (dd, J_{MA}=*18.4 Hz*, J_{MX}=*5.8 Hz*, H_M), 5.368 (d, J_{MX}=*3.8 Hz*, H_X), 6.607-7.572 (m, Ar-H, 7H), 8.956 & 10.201 (2s, 2Ar-OH, 2H); ^{13}C-NMR (400 MHz, DMSO-d_6) δ (ppm) 22.43, 44.13, 56.25, 58.55, 112.92, 116.81, 120.18, 129.64, 132.42, 135.49, 147.37, 156.39, 157.30, 167.39; HRMS (m/z) calcd. for $C_{18}H_{18}N_2O_4$ $(M+H)^+$ 327.1345, found 327.1340.

***1-(5-(2-chlorophenyl)-3-(2-hydroxyphenyl)-4,5-dihydro-1H-pyrazol-1-yl) ethan-1one* (25)**

White amorphous powder; yield: 70%; mp (°C): 178-181; ^{1}H-NMR (400 MHz, DMSO-d_6) δ (ppm) 2.340 (s, -C(=O)-CH_3, 3H) 3.176 (dd, J_{AM}=*18.2 Hz*, J_{AX}=*2.6 Hz*, H_A), 4.049 (dd,

J_{MA}=*18.4 Hz*, J_{MX}=*2.6 Hz*, H_M), 5.720 (dd, J_{MX}=*11.8 Hz*, J_{AX}=*2.6 Hz*, H_X), 6.890-7.585 (m, Ar-H, 8H), 10.159 (s, Ar-OH, H); ^{13}C-NMR (400 MHz, DMSO-d_6) δ (ppm) 22.34, 43.23, 56.93, 116.84, 120.15, 126.95, 128.23, 129.60, 130.30, 131.30, 132.50, 139.28, 156.20, 157.29, 167.76; HRMS (m/z) calcd. for $C_{17}H_{15}ClN_2O_2$ $(M+H)^+$ 315.0900, found 315.0896.

1-(5-(3-chlorophenyl)-3-(2-hydroxyphenyl)-4,5-dihydro-1H-pyrazol-1-yl) ethan-1one **(26)**

White amorphous powder; yield: 65%; mp (°C): 159-161; ^{1}H-NMR (400 MHz, DMSO-d_6) δ (ppm) 2.301 (s, -C(=O)-CH_3, 3H) 3.260 (d, J_{AM}=*2.4 Hz*, H_A), 3.962 (dd, J_{MA}=*18.4 Hz*, J_{MX}=*5.8 Hz*, H_M), 5.515 (dd, J_{MX}=*12.0 Hz*, J_{AX}=*2.2 Hz*, H_X), 6.905-7.575 (m, Ar-H, 8H), 10.165 (s, Ar-OH, H); ^{13}C-NMR (400 MHz, DMSO-d_6) δ (ppm) 22.36, 44.12, 58.56, 116.77, 120.04, 124.68, 126.14, 127.85, 129.66, 131.26, 132.49, 133.80, 145.21, 156.19, 157.30 167.82; HRMS (m/z) calcd. for $C_{17}H_{15}ClN_2O_2$ $(M+H)^+$ 315.0900, found 315.0898.

1-(5-(4-chlorophenyl)-3-(2-hydroxyphenyl)-4,5-dihydro-1H-pyrazol-1-yl) ethan-1one **(27)**

White amorphous powder; yield: 71%; mp (°C): 137-140; ^{1}H-NMR (400 MHz, DMSO-d_6) δ (ppm) 2.286 (s, -C(=O)-CH_3, 3H) 3.257 (dd, J_{AM}=*18.4 Hz*, J_{AX}=*2.4 Hz*, H_A), 3.959 (dd, J_{MA}=*18.4 Hz*, J_{MX}=*5.8 Hz*, H_M), 5.509 (dd, J_{MX}=*11.8 Hz*, J_{AX}=*2.2 Hz*, H_X), 6.904-7.575 (m, Ar-H, 8H), 10.164 (s, Ar-OH, H); ^{13}C-NMR (400 MHz, DMSO-d_6) δ (ppm) 22.34, 44.09, 58.32, 116.95, 119.93, 128.12, 129.05, 129.62, 132.46, 141.73, 156.16, 157.29, 167.67; HRMS (m/z) calcd. for $C_{17}H_{15}ClN_2O_2$ $(M+H)^+$ 315.0900, found 315.0897.

1-(5-(2-fluorophenyl)-3-(2-hydroxyphenyl)-4,5-dihydro-1H-pyrazol-1-yl) ethan-1one **(28)**

White amorphous powder; yield: 81%; mp (°C): 145-147; ^{1}H-NMR (400 MHz, DMSO-d_6) δ (ppm) 2.294 (s, -C(=O)-CH_3, 3H) 3.261 (d, J_{AM}=*2.4 Hz*, H_A), 3.996 (dd, J_{MA}=*18.2 Hz*, J_{MX}=*6.2 Hz*, H_M), 5.643 (dd, J_{MX}=*12.2 Hz*, J_{AX}=*2.4 Hz*, H_X), 6.903-7.585 (m, Ar-H, 8H), 10.168 (s, Ar-OH, H); ^{13}C-NMR (400 MHz, DMSO-d_6) δ (ppm) 22.33, 43.21, 53.96, 116.14, 117.11, 120.17, 125.04, 128.16, 129.22, 129.92, 132.50, 156.36, 157.30, 158.68, 161.12, 167.68; HRMS (m/z) calcd. for $C_{17}H_{15}FN_2O_2$ $(M+H)^+$ 299.1196, found 299.1199.

1-(5-(3-fluorophenyl)-3-(2-hydroxyphenyl)-4,5-dihydro-1H-pyrazol-1-yl) ethan-1one **(29)**

White amorphous powder; yield: 78%; mp (°C): 131-133; ^{1}H-NMR (400 MHz, DMSO-d_6) δ (ppm) 2.304 (s, -C(=O)-CH_3, 3H) 3.250 (d, J_{AM}=*2.4 Hz*, H_A), 3.963 (dd, J_{MA}=*18.4 Hz*, J_{MX}=*6.0 Hz*, H_M), 5.529 (dd, J_{MX}=*11.8 Hz*, J_{AX}=*2.4 Hz*, H_X), 6.902-7.575 (m, Ar-H, 8H), 10.168 (s, Ar-OH, H); ^{13}C-NMR (400 MHz, DMSO-d_6) δ (ppm) 22.34, 43.95, 58.56, 113.14, 114.52, 116.77, 120.12, 122.04, 129.63, 131.28, 132.45, 145.57, 156.14, 157.29, 161.66, 164.08, 167.77; HRMS (m/z) calcd. for $C_{17}H_{15}FN_2O_2$ $(M+H)^+$ 299.1196, found 299.1200.

1-(5-(4-fluorophenyl)-3-(2-hydroxyphenyl)-4,5-dihydro-1H-pyrazol-1-yl) ethan-1one **(30)**

White amorphous powder; yield: 83%; mp (°C): 136-138; ^{1}H-NMR (400 MHz, DMSO-d_6) δ (ppm) 2.269 (s, -C(=O)-CH_3, 3H) 3.261 (dd, J_{AM}=*18.4 2.2 Hz*, H_A), 3.952 (dd, J_{MA}=*18.4 Hz*, J_{MX}= *6.0 Hz*, H_M), 5.515 (dd, J_{MX}=*11.6 Hz*, J_{AX}=*2.2 Hz*, H_X), 6.906-7.576 (m, Ar-H, 8H), 10.176 (s, Ar-OH, H); ^{13}CNMR (400 MHz, DMSO-d_6) δ (ppm) 22.37, 44.17, 58.45, 114.53, 115.84, 116.92, 120.13, 127.38, 128.16, 129.63, 132.44, 138.97, 156.19, 157.30, 160.64, 163.05, 167.63; HRMS (m/z) calcd. for $C_{17}H_{15}FN_2O_2$ $(M+H)^+$ 299.1196, found 299.1196.

1-(5-(2-bromophenyl)-3-(2-hydroxyphenyl)-4,5-dihydro-1H-pyrazol-1-yl) ethan-1one **(31)**

White amorphous powder; yield: 76%; mp (°C): 168-170; ^{1}H-NMR (400 MHz, DMSO-d_6) δ (ppm) 2.344 (s, -C(=O)-CH_3, 3H) 3.149 (dd, J_{AM}=*18.0 Hz*, J_{AX}=*2.4 Hz*, H_A), 4.051 (dd, J_{MA}=*18.4 Hz*, J_{MX}=*6.0 Hz*, H_M), 5.679 (dd, J_{MX}=*11.8 Hz*, J_{AX}=*2.4 Hz*, H_X), 6.887-7.676 (m, Ar-H, 8H), 10.155 (s, Ar-OH, H); ^{13}C-NMR (400 MHz, DMSO-d_6) δ (ppm) 22.27, 43.39, 59.05, 116.86, 120.14, 121.46, 126.65, 128.80, 129.60, 132.50, 133.51, 140.92, 156.04, 167.74; HRMS (m/z) calcd. for $C_{17}H_{15}BrN_2O_2$ $(M+H)^+$ 359.0395, found 359.0386.

1-(5-(3-bromophenyl)-3-(2-hydroxyphenyl)-4,5-dihydro-1H-pyrazol-1-yl) ethan-1one **(32)**

White amorphous powder; yield: 72%; mp (°C): 177-179; ^{1}H-NMR (400 MHz, DMSO-d_6) δ (ppm) 2.299 (s, -C(=O)-CH_3, 3H) 3.261 (d, J_{AM}=*2.4 Hz*, H_A), 3.957 (dd, J_{MA}=*18.4 Hz*, J_{MX}= *6.0 Hz*, H_M), 5.505 (dd, J_{MX}= *12.0 Hz*, J_{AX}=*2.4 Hz*, H_X), 6.906-7.575 (m, Ar-H, 8H), 10.105 (s, Ar-OH, H); ^{13}C-NMR (400 MHz, DMSO-d_6) δ (ppm) 22.34, 44.13, 58.51, 116.75, 117.07, 120.14, 122.39, 125.04, 129.01, 129.65, 130.74, 131.54, 132.48, 145.43, 156.19, 157.29, 167.83; HRMS (m/z) calcd. for $C_{17}H_{15}BrN_2O_2$ $(M+H)^+$ 359.0395, found 359.0396.

1-(5-(4-bromophenyl)-3-(2-hydroxyphenyl)-4,5-dihydro-1H-pyrazol-1-yl) ethan-1one **(33)**

White amorphous powder; yield: 81%; mp (°C): 154-156; ^{1}H-NMR (400 MHz, DMSO-d_6) δ (ppm) 2.285 (s, -C(=O)-CH_3, 3H) 3.256 (dd, J_{AM}= *18.4 Hz*, J_{AX}=*2.4 Hz*, H_A), 3.957 (dd, J_{MA}= *18.4 Hz*, J_{MX}= *6.0 Hz*, H_M), 5.491 (dd, J_{MX}= *11.6 Hz*, J_{AX}= *2.2 Hz*, H_X), 6.904-7.573 (m, Ar-H, 8H), 10.163 (s, Ar-OH, H); ^{13}C-NMR (400 MHz, DMSO-d_6) δ (ppm) 22.34, 43.88, 58.52, 116.76, 117.07, 120.14, 120.92, 128.46, 129.62, 132.10, 132.48, 142.15, 156.17, 157.28, 167.70; HRMS (m/z) calcd. for $C_{17}H_{15}BrN_2O_2$ $(M+H)^+$ 359.0395, found 359.0395.

General procedure for synthesis of 3,5-diaryl-4,5-dihydro-1H-pyrazoles (34-49)

A solution of the appropriate chalcone (0.10 mM) and excess hydrazine hydrate (0.15 mM) in ethanol was refluxed for 6-8 h. The hot reaction mixture was then poured into 50 g crushed ice. The crude white precipitate thus obtained was then filtered, washed with water and dried. The product was recrystallized from ethanol.

2-(5-phenyl)-4,5-dihydro-1H-pyrazol-3-yl)phenol **(34)**

Gray amorphous powder; yield: 65%; mp (°C): 105-106; ^{1}H-NMR (300 MHz, DMSO-d_6) δ (ppm) 2.995 (dd, J_{AM}*=16.5 Hz*, J_{AX}*=5.4 Hz*, H_A), 3.625 (dd, J_{MA}*=16.7 Hz*, J_{MX}*=5.4 Hz*, H_M), 4.854 (appeared as t, J_{MX}*=10.8 Hz*, H_X), 6.857-8.059 (m, Ar-H, 9H), 7.845 (s, ring-NH, 1H) 11.160 (s, Ar-OH, 1H); ^{13}C-NMR (125 MHz, $CDCl_3$) δ (ppm) 41.75, 62.84, 116.58, 116.74, 119.22, 126.47, 127.72, 128.20, 129.14, 130.59, 142.20, 154.33, 157.90; HRMS (m/z) calcd. for $C_{15}H_{14}N_2O$ $(M+H)^+$ 239.1184, found 239.1185.

***2,2'-(4,5-dihydro-1H-pyrazol-3,5-diyl)diphenol* (35)**

White amorphous powder; yield: 67%; mp (°C): 133-136; ^{1}H-NMR (400 MHz, DMSO-d_6) δ (ppm) 2.902 (dd, J_{AM}*=16.4 Hz*, J_{AX}*=5.0 Hz*, H_A), 3.571 (dd, J_{MA}*=16.6 Hz*, J_{MX}*=5.2 Hz*, H_M), 5.019 (appeared as t, J_{MX}*=10.0 Hz*, H_X), 6.758-7.640 (m, Ar-H, 8H), 7.640 (s, ring-NH, 1H) 9.610 & 11.213 (2s, 2Ar-OH, 2H); ^{13}C-NMR (125 MHz, CD_3OD) δ (ppm) 40.50, 59.71, 116.42, 117.09, 117.95, 120.26, 120.61, 128.00, 128.18, 129.08, 129.60, 131.32, 156.54, 157.63, 158.84; HRMS (m/z) calcd. for $C_{15}H_{14}N_2O_2$ $(M+H)^+$ 255.1134, found 255.1140.

***2-(5-(3-hydroxyphenyl)-4,5-dihydro-1H-pyrazol-3-yl)phenol* (36)**

White amorphous powder; yield: 63%; mp (°C): 166-168; ^{1}H-NMR (300 MHz, DMSO-d_6) δ (ppm) 2.927 (dd, J_{AM}*=12.6 Hz*, J_{AX}*= 4.1 Hz*, H_A), 3.512 (dd, J_{MA}*= 12.2 Hz*, J_{MX}*= 3.9 Hz*, H_M), 4.711 (dd, J_{MX}*= 16.5 Hz*, J_{AX}*= 4.2 Hz*, H_X), 6.708-7.285 (m, Ar-H, 8H), 7.713 (s, ring-NH, 1H) 9.348 & 11.178 (2s, 2Ar-OH, 2H); ^{13}C-NMR (125 MHz, CD_3OD) δ (ppm) 42.34, 63.85, 114.21, 115.62, 117.06, 117.97, 118.76, 120.26, 128.92, 130.80, 131.18, 145.11, 155.86, 158.79, 158.89; HRMS (m/z) calcd. for $C_{15}H_{14}N_2O_2$ $(M+H)^+$ 255.1134, found 255.1139.

***2-(5-(4-hydroxyphenyl)-4,5-dihydro-1H-pyrazol-3-yl)phenol* (37)**

White amorphous powder; yield: 69%; mp (°C): 109-111; ^{1}H-NMR (400 MHz, DMSO-d_6) δ (ppm) 2.944 (dd, J_{AM}*= 16.6 Hz*, J_{AX}*= 5.4 Hz*, H_A), 3.530 (dd, J_{MA}*= 16.4 Hz*, J_{MX}*= 5.2 Hz*, H_M), 4.744 (dd, J_{MX}*= 10.6 Hz*, J_{AX}*= 3.6 Hz*, H_X), 6.723-7.303 (m, Ar-H, 8H), 7.704 (s, ring-NH, 1H) 9.335 & 11.181 (2s, 2Ar-OH, 2H); ^{13}C-NMR (125 MHz, CD_3OD) δ (ppm) 42.21, 63.67, 116.41, 117.06, 118.01, 120.25, 128.86, 128.94, 131.17, 133.97, 156.23, 158.19, 158.81; HRMS (m/z) calcd. for $C_{15}H_{14}N_2O_2$ $(M+H)^+$ 255.1134, found 255.1138.

***2-(5-(o-tolyl)-4,5-dihydro-1H-pyrazol-3-yl)phenol* (38)**

Off-white amorphous powder; yield: 62%; mp (°C): 98-99; ^{1}H-NMR (300 MHz, DMSO-d_6) δ (ppm) 2.340 (s, Ar-CH_3, 3H), 2.865 (dd, J_{AM}*=16.8 Hz*, J_{AX}*= 5.1 Hz*, H_A), 3.678 (dd, J_{MA}*= 16.8 Hz*, J_{MX}*= 5.4 Hz*, H_M), 5.019 (appeared as split t, J_{MX}*= 10.5 Hz*, H_X), 6.847-7.455 (m, Ar-H, 8H), 7.768 (s, ring-NH, 1H) 11.185 (s, Ar-OH, 1H); ^{13}C-NMR (125 MHz, $CDCl_3$) δ (ppm) 19.64, 40.46, 59.26, 116.67, 116.71, 119.19, 125.36, 126.90, 127.66, 127.81, 130.52, 130.84,

135.07, 140.10, 154.00, 157.86; HRMS (m/z) calcd. for $C_{16}H_{16}N_2O$ $(M+H)^+$ 253.1341, found 253.1350.

***2-(5-(p-tolyl)-4,5-dihydro-1H-pyrazol-3-yl)phenol* (39)**

Pale brown crystalline powder; yield: 61%; mp (°C): 105-106; ^{1}H-NMR (400 MHz, DMSO-d_6) δ (ppm) 2.287 (s, Ar-CH_3, 3H), 2.964 (dd, J_{AM}= *16.8 Hz*, J_{AX}= *5.4 Hz*, H_A), 3.586 (dd, J_{MA}=*16.6 Hz*, J_{MX}=*5.2 Hz*, H_M), 4.811 (appeared as t, J_{MX}=*10.8 Hz*, H_X), 6.861-7.495 (m, Ar-H, 8H), 7.821 (s, ring-NH, 1H) 11.165 (s, Ar-OH, 1H); ^{13}C-NMR (125 MHz, CD_3OD) δ (ppm) 21.13, 42.29, 63.75, 117.05, 117.95, 120.23, 127.57, 128.89, 130.32, 131.17, 138.48, 140.31, 155.98, 158.76; HRMS (m/z) calcd. for $C_{16}H_{16}N_2O$ $(M+H)^+$ 253.1341, found 253.1338.

***2-(5-(2-methoxyphenyl)-4,5-dihydro-1H-pyrazol-3-yl)phenol* (40)**

Pale brown amorphous powder; yield: 64%; mp (°C): 121-123; ^{1}H-NMR (300 MHz, DMSO-d_6) δ (ppm) 3.578 (dd, J_{AM}=*16.7 Hz*, J_{AX}=*5.3 Hz*, H_A), 3.930 (appeared as d, J_{MA}=*1.1 Hz*, H_M), 3.828 (s, Ar-OCH_3, 3H) 5.037 (appeared as split t, J_{MX}=*10.4 Hz*, H_X), 6.840-7.386 (m, Ar-H, 8H), 7.672 (s, ring-NH, 1H) 11.201 (s, Ar-OH, 1H); ESI-MS (m/z) calcd. for $C_{16}H_{16}N_2O_2$ $(M+H)^+$ 269.1290, found 269.

***2-(5-(4-methoxyphenyl)-4,5-dihydro-1H-pyrazol-3-yl)phenol* (41)**

Pale brown amorphous powder; yield: 77%; mp (°C): 92-94; ^{1}H-NMR (400 MHz, DMSO-d_6) δ (ppm) 2.960 (dd, J_{AM}=*16.4 Hz*, J_{AX}=*5.4 Hz*, H_A), 3.564 (dd, J_{MA}=*16.6 Hz*, J_{MX}=*5.2 Hz*, H_M), 3.739 (s, Ar-OCH_3, 3H) 4.796 (dd, J_{MX}=*17.8 Hz*, J_{AX}=*1.8 Hz*, H_X), 6.861-7.335 (m, Ar-H, 8H), 7.769 (s, ring NH, 1H) 10.187 (s, Ar-OH, 1H); ^{13}C-NMR (125 MHz, CD_3OD) δ (ppm) 42.27, 55.70, 63.56, 115.08, 117.07, 118.00, 120.26, 128.85, 128.93, 131.19, 135.25, 156.10, 158.81, 160.77; HRMS (m/z) calcd. for $C_{16}H_{16}N_2O_2$ $(M+H)^+$ 269.1290, found 269.1296.

***5-(3-(2-hydroxyphenyl)-4,5-dihydro-1H-pyrazol-5-yl)-2-methoxyphenol* (42)**

White amorphous powder; yield: 71%; mp (°C): 142-144; ^{1}H-NMR (400 MHz, DMSO-d_6) δ (ppm) 2.936 (dd, J_{AM}=*16.6 Hz*, J_{AX}=*5.2 Hz*, H_A), 3.535 (dd, J_{MA}=*16.6 Hz*, J_{MX}=*5.2 Hz*, H_M), 3.740 (s, Ar-OCH_3, 3H) 4.712 (appeared as t, J_{MX}=*10.0 Hz*, H_X), 6.742-7.301 (m, Ar-H, 7H), 7.716 (s, ring-NH, 1H), 8.953 & 11.187 (2s, 2Ar-OH, 2H); ^{13}C-NMR (125 MHz, CD_3OD) δ (ppm) 42.26, 56.43, 63.61, 112.79, 114.46, 117.05, 118.01, 118.95, 120.26, 128.93, 131.18, 136.31, 147.85, 148.70, 156.07, 158.81; HRMS (m/z) calcd. for $C_{16}H_{16}N_2O_3$ $(M+H)^+$ 285.1239, found 285.1236.

***2-(5-(2-chlorophenyl)-4,5-dihydro-1H-pyrazol-3-yl)phenol* (43)**

White crystalline powder; yield: 66%; mp (°C): 74-77; ^{1}H-NMR (300 MHz, DMSO-d_6) δ (ppm) 2.917 (dd, J_{AM}=*16.8 Hz*, J_{AX}=*5.0 Hz*, H_A), 3.750 (dd, J_{MA}=*16.8 Hz*, J_{MX}=*5.4 Hz*, H_M), 5.133 (appeared as split t, J_{MX}=*10.5 Hz*, H_X), 6.844-7.613 (m, Ar-H, 8H), 7.878 (s, ring-NH, 1H),

11.086 (s, Ar-OH, 1H); ^{13}C-NMR (125 MHz, CD_3OD) δ (ppm) 41.22, 60.56, 117.06, 117.89, 120.28, 128.50, 128.53, 128.84, 129.95, 130.65, 131.18, 133.96, 141.01, 155.01 158.73; HRMS (m/z) calcd. for $C_{15}H_{13}ClN_2O$ $(M+H)^+$ 273.0795, found 273.0795.

***2-(5-(4-chlorophenyl)-4,5-dihydro-1H-pyrazol-3-yl)phenol* (44)**

White crystalline powder; yield: 73%; mp (°C): 128-131; ^{1}H-NMR (400 MHz, DMSO-d_6) δ (ppm) 2.980 (dd, J_{AM}*=16.6 Hz*, J_{AX}*=5.4 Hz*, H_A), 3.633 (dd, J_{MA}*=16.8 Hz*, J_{MX}*=5.4 Hz*, H_M), 4.851 (dd, J_{MX}*=22.6 Hz*, J_{AX}*=6.4 Hz*, H_X), 6.886-7.706 (m, Ar-H, 8H), 7.860 (s, ring-NH, 1H), 11.101 (s, Ar-OH, 1H); ^{13}C-NMR (125 MHz, CD_3OD) δ (ppm) 42.43, 63.35, 117.09, 117.88, 120.27, 128.91, 129.42, 129.78, 131.24, 134.36, 142.35, 155.66, 158.79; HRMS (m/z) calcd. for $C_{15}H_{13}ClN_2O$ $(M+H)^+$ 273.0795, found 273.0800.

***2-(5-(2-fluorophenyl)-4,5-dihydro-1H-pyrazol-3-yl)phenol* (45)**

White amorphous powder; yield: 73%; mp (°C): 104-106; ^{1}H-NMR (400 MHz, DMSO-d_6) δ (ppm) 3.034 (dd, J_{AM}*=16.4 Hz*, J_{AX}*=5.0 Hz*, H_A), 3.662 (dd, J_{MA}*=16.8 Hz*, J_{MX}*=5.4 Hz*, H_M), 5.053 (appeared as t, J_{MX}*=10.4 Hz*, H_X), 6.864-7.522 (m, Ar-H, 8H), 7.811 (s, ring-NH, 1H), 11.102 (s, Ar-OH, 1H); ^{13}C-NMR (125 MHz, CD_3OD) δ (ppm) 41.07, 57.30, 116.37, 117.08, 117.87, 120.28, 125.62, 128.90, 128.92, 130.24, 130.39, 131.25, 155.75, 158.77, 162.03; HRMS (m/z) calcd. for $C_{15}H_{13}FN_2O$ $(M+H)^+$ 257.1090, found 257.1092.

***2-(5-(3-fluorophenyl)-4,5-dihydro-1H-pyrazol-3-yl)phenol* (46)**

Off-white amorphous powder; yield: 79%; mp (°C): 65-67; ^{1}H-NMR (400 MHz, DMSO-d_6) δ (ppm) 3.012 (dd, J_{AM}*=16.8 Hz*, J_{AX}*=5.4 Hz*, H_A), 3.645 (dd, J_{MA}*=16.8 Hz*, J_{MX}*=5.4 Hz*, H_M), 4.890 (appeared as d, J_{MX}*=10.8 Hz*, H_X), 6.867-7.519 (m, Ar-H, 8H), 7.885 (s, ring-NH, 1H), 11.095 (s, Ar-OH, 1H); ESI-MS (m/z) calcd. For $C_{15}H_{13}FN_2O$ $(M+H)^+$ 257.1090, found 257.

***2-(5-(4-fluorophenyl)-4,5-dihydro-1H-pyrazol-3-yl)phenol* (47)**

White amorphous powder; yield: 79%; mp (°C): 94-96; ^{1}H-NMR (300 MHz, DMSO-d_6) δ (ppm) 2.981 (dd, J_{AM}*=16.7 Hz*, J_{AX}*=5.1 Hz*, H_A), 3.619 (dd, J_{MA}*=16.7 Hz*, J_{MX}*=5.3 Hz*, H_M), 4.868 (appeared as split t, J_{MX}*=10.7 Hz*, H_X), 6.859-7.471 (m, Ar-H, 8H), 7.843 (s, ring-NH, 1H), 11.121 (s, ArOH, 1H); ^{13}C-NMR (125 MHz, $CDCl_3$) δ (ppm) 41.89, 62.26, 115.97, 116.46, 116.78, 119.26, 127.70, 128.22, 130.69, 137.86, 154.34, 157.89, 162.58; HRMS (m/z) calcd. for $C_{15}H_{13}FN_2O$ $(M+H)^+$ 257.1090, found 257.1092.

***2-(5-(2-bromophenyl)-4,5-dihydro-1H-pyrazol-3-yl)phenol* (48)**

White amorphous powder; yield: 63%; mp (°C): 131-133; ^{1}H-NMR (300 MHz, DMSO-d_6) δ (ppm) 2.893 (dd, J_{AM}*=16.8 Hz*, J_{AX}*=5.0 Hz*, H_A), 3.756 (dd, J_{MA}*=16.8 Hz*, J_{MX}*=5.6 Hz*, H_M), 5.091 (appeared as split t, J_{MX}*=10.4 Hz*, H_X), 6.843-7.668 (m, Ar-H, 8H), 7.898 (s, ring-NH, 1H), 11.073 (s, ArOH, 1H); ^{13}C-NMR (125 MHz, $CDCl_3$) δ (ppm) 40.43, 61.86, 116.50,

116.74, 119.26, 123.12, 127.43, 127.77, 128.23, 129.44, 130.68, 133.16, 140.97, 154.23, 157.87; HRMS (m/z) calcd. for $C_{15}H_{13}BrN_2O$ $(M+H)^+$ 317.0290, found 317.0287.

***2-(5-(4-bromophenyl)-4,5-dihydro-1H-pyrazol-3-yl)phenol* (49)**

White crystalline powder; yield: 68%; mp (°C): 144-146; ^{1}H-NMR (400 MHz, DMSO-d_6) δ (ppm) 2.978 (dd, J_{AM}*=16.8 Hz*, J_{AX}*=5.4 Hz*, H_A), 3.632 (dd, J_{MA}*=16.6 Hz*, J_{MX}*=5.2 Hz*, H_M), 4.851 (appeared as split t, J_{MX}*=8.1 Hz*, H_X), 6.866-7.642 (m, Ar-H, 8H), 7.862 (s, ring-NH, 1H), 11.097 (s, Ar-OH, 1H); ^{13}C-NMR (125 MHz, CD_3OD) δ (ppm) 42.23, 62.94, 116.87, 117.39, 120.04, 122.15, 128.53, 129.25, 131.04, 132.55, 142.16, 155.29, 158.25; HRMS (m/z) calcd. for $C_{15}H_{13}BrN_2O$ $(M+H)^+$ 317.0290, found 317.0276.

Anti-mycobacterial activity.

The resazurin microtitre assay was used to assess the minimum inhibitory concentration (MIC_{90}) of compounds against *M. smegmatis*, *M. aurum*, *M. bovis* BCG and *M. tuberculosis*.[20] The assay was conducted in a semi-automated standard 96-well plate format. In order to determine the minimum inhibitory concentration (MIC_{90}, that inhibited >90% growth), the designed analogs were screened under iron-deficient (GAST) and standard iron-rich (GAST-Fe, supplemented with 200 μM $FeCl_3$) media. Stock solutions of test compounds **1**-**49** were prepared in DMSO to a concentration of 10 mg/mL. Rifampicin and isoniazid were used as standards for the study. The concentration range 0.5-256 μg/mL was used for all test compounds in both media. All working concentrations were inoculated with a culture concentration of 10^5 colony forming units (CFU)/mL of appropriate mycobacterial strains. The inhibitory potential of the compounds was assessed after an incubation period of 24 h (*M. smegmatis*), 72 h (*M. aurum*), 5 days (*M. bovis* BCG) and 8 days (*M. tuberculosis*) at 37 °C in static conditions. 20 μL of (0.01% w/v) resazurin solution was then added and cells were incubated at 37 °C for 4 h and 12 h for *M. smegmatis* and *M. aurum* whereas 24 h for both *M. bovis* BCG and *M. tuberculosis*, respectively. The colorimetric change (blue to pink) was measured using at excitation 530 nm and emission 590 nm. The assay is based on the formation of fluorescent resorufin (pink) from nonfluorescent resazurin (blue) under the reductase activity of viable cells in each well. Assays were performed in biological triplicate. TSI[20] was calculated using:

$$\textit{Target Specificity Index (TSI)} = \frac{MIC_{90}\ in\ GAS{-}Fe\ medium}{MIC_{90}\ in\ GAS\ medium}$$

X-Ray Crystallography & Hirshfeld surface analysis of 44 and 49.

Compounds **44** and **49** were crystallized from ethanol by concentration followed by cooling overnight in ice. Single crystal X-ray data for compounds **44** and **49** was collected using

graphite monochromated Mo-K_α radiation (λ = 0.71073 Å). Data collection was performed with the Bruker APEX2 suite.[58] Unit-cell parameter refinement, data integration and reduction were done using the SAINT program and absorption correction was done using the SADABS program.[59] Structures were solved using direct methods and refined with a full-matrix least-squares method on F^2 using SHELXL-2018 in WinGX programs suite.[60,61] All non-hydrogen atoms were refined anisotropically where the positions of the hydrogen atoms were calculated from known geometry (bond lengths of C-H for aromatic, methylene and methyl atoms are 0.93, 0.97, and 0.96 Å, respectively).

Hirshfeld surface analysis offers an overview of the space occupied by each molecule in the crystal and can be used to analyse all intermolecular interactions between compounds in a crystal lattice. Hirshfeld surface analysis was performed using the Crystalexplorer 17.5 package.[62,63] The normalized contact distance (d_{norm}) based on the van der Waals radii were mapped into Hirshfeld surfaces where negative and positive values of d_{norm} indicate whether intermolecular contacts are shorter (red color) or longer (blue color) than the van der Waals separations respectively.

Estimation of siderophore production.

Inhibition of siderophore production was measured using the universal CAS liquid assay.[64] *M. smegmatis* cells were grown in GAST medium and diluted to an optical density (OD_{630}) of 0.01 in chelated GAST medium.[26] First, siderophore production was measured at various iron concentrations (0-200 µM) by checking OD at 630 nm using supernatant solution (100 µL) and addition of CAS assay liquid solution (100 µL) to each well. The assay was then carried out in the presence of test compounds (**44** and **49**) in a 96-well plate format using test concentrations 1 x MIC_{90} (4 µg/mL) for 3 h. Treated bacterial culture with test compounds (100 µL) was added to 96 well plates followed by the addition of CAS assay liquid solution (100 µL). Supernatant solution from untreated bacterial culture (100 µL) with CAS assay liquid solution (100 µL) was used as a control. Plates were incubated for 10 min at room temperature and absorbance was read at 630 nm. The experiment was performed in triplicate for each sample.

$$\text{Siderophore units (SU)} = ((A_r - A_s) * 100)/A_r$$

A_r - absorbance at 630 nm of the blank with CAS assay solution.

A_s - absorbance of test culture supernatant with CAS assay solution.

Determination of mode of action.

The HT-SPOTi agar based method was used to determine the mode of action of the potent compounds using *M. smegmatis* as surrogate bacteria model.[25, 65] The assay was conducted in

a semiautomated 96-well plate format. To each well of a 96-well plate, 198 μL agar and 2 μL of drugs were added. To all plates 2 μL of early to mid-log bacterial culture containing 2×10^3 colony forming units (CFUs) was spotted in the middle of each well. Plates were incubated for 48 h at 37 ºC. The MIC_{90} was determined as the lowest concentration of the compound where mycobacterial growth was completely inhibited on the agar. Following this, the surface of the agar was scraped from the MIC well and transferred into GAST medium. This was incubated for 5 days at 37 ºC in a shaking incubator at 180 rpm, and further plating was done on agar plates to monitor growth by naked eye.

Cytotoxicity assay.

The cytotoxicity assay was performed according to published procedures.[44,48] The cell lines, confluent murine macrophage cells RAW 264.7 and THP-1 cells, were grown and maintained in RPMI-1640 supplemented with 10% FBS at 37 °C in a humidified incubator with 5% CO_2. 2nd passage of the cell-lines was used for the assays. For cytotoxicity determination, 2 μL of a 50 mg/mL stock solution of each compound was diluted in 200 μL of RPMI-1640 medium in the first row of a 96-well microplate, and 2-fold dilutions were performed along the rows, leaving the last row as a media control. Then 100 μL of RAW 264.7 and THP-1 cells (5×10^5 cells/mL) in logarithmic growth phase were added to each well. The plates were incubated at 37 °C in a humidified incubator with 5% CO_2 for 48 h. To avoid the large loss of THP-1 cells and detachment upon washing, THP-1 96-well plates were centrifuged at 1200 rpm for 5 minutes using a Thermo scientific 75003624 M-20 rotor, in a Heraeus Megafuge 16R centrifuge. After centrifugation, each well was washed twice with 1x PBS, followed by the addition of fresh RPMI-1640 containing 10% FBS (170 μL) to each well. 30 μL of 0.01% resazurin solution was then added to each well and plates were incubated at 37 °C in a humidified incubator with 5% CO_2 overnight. The change in color was observed and fluorescence intensity was measured at excitation 560 nm and emission 590 nm. The assays were performed in biological triplicate. The selectivity index (SI) was calculated using:

$$Selectivity\ Index\ (SI) = \frac{Cell\ Inhibition\ Concentration}{MIC_{90}\ in\ GAS\ medium}$$

Antimycobacterial activity in macrophage infection model.

In the killing assay, RAW 264.7 mouse macrophages (5×10^5) were infected with *M. aurum* at 10:1 multiplicity of infection (moi) for 1 h at 37 °C in a 24-well plate. The culture was washed with RPMI-1640 three times and then incubated with different concentrations (concentration range 1-16 μg/mL) of **44** and **49** in complete RPMI medium. Cultures were incubated for four different times: 2 h, 24 h, 48 h, and 72 h. After the stipulated time, cells were washed twice

with RPMI-1640 medium and lysed in 500 µL of distilled water at rt using a rubber plunger for 10 min. Lysed cells were centrifuged and resuspended in 50 µL of distilled water. From the cell suspension 5 µL was spotted onto wells of 24-well plate containing 2 ml MB 7H10 agar supplemented with 10% OADC. Plates were incubated at 37 °C for 5 days to determine the intracellular survival of *M. aurum* in the presence of different concentrations of inhibitor.

Checkerboard assay for drug-drug interactions.

The HT-SPOTi assay was modified for this experiment. Each combination of drug was tested on a separate 96-well microtitre plate using *M. smegmatis*. Concentrations ranging from 1/8 x - 8 x MIC of each drug was tested. 1 µL of the dilutions from the DMSO stock solution of drugs were added along the rows. Similarly, 1 µL of the dilutions from the working stocks of the second drug were added along the columns. This creates a checkerboard of different concentration of the drugs to evaluate drug-drug synergism/antagonism profile. The fractional inhibitory concentration index (FICI) was calculated for each antibiotic in each combination using:

$$FIC_A + FIC_B = FICI$$

$$FIC_A = \frac{MIC_{90}\ of\ combination\ of\ drug\ A\ and\ B}{MIC_{90}\ of\ drug\ A\ alone}$$

$$FIC_B = \frac{MIC_{90}\ of\ combination\ of\ drug\ A\ and\ B}{MIC_{90}\ of\ drug\ B\ alone}$$

The FICIs were interpreted as follows: synergy, FICI of ≤ 0.5; additivity, FICI of >0.5 to ≤1; no interaction (indifference), FICI of >1 to ≤4; antagonism, FICI of >4.

Enzyme-inhibitor interaction study using Thermofluorimetry.

Fluorescence-thermal shift assays were carried out in a 96-well plate format using the MyIQ instrument (Bio-Rad). Purified MbtA was first diluted to a concentration of 20 µM with different buffers: 50 mM Mes pH 6.5 100 mM NaCl or 500 mM NaCl; 50 mM Hepes pH 7.5 100 mM NaCl or 500 mM NaCl; 50 mM Tris pH 8.5 100 mM NaCl or 500 mM NaCl. These buffers had already been supplemented with 3 mM $MgCl_2$ and 1 mM ATP. 25 µL reactions were set up with 10 µM MbtA and a 1/500 dilution of 5000x SYPRO Orange (Invitrogen). Depending on the experiment, 1% DMSO or 100 µM inhibitor (**1**, **44** and **49**) prepared at a final concentration of 1% DMSO were also added and incubated for 1 h at 4 ℃. The plates were sealed, centrifuged for 5 min and relative fluorescence was recorded at a rate of 0.5 °C min^{-1} from 25 ℃ to 95 ℃. Each experiment was conducted in triplicate. Note: the presence of $MgCl_2$ or ATP did not affect the melting curve (data not shown).

Molecular docking and Molecular dynamics.

Docking. In order to understand the molecular level interaction molecular docking studies were performed using AutoDock 4.2 (The Scripps Research Institute) and RHEL-5.0 Operating system (Dell Precision workstation with Intel core 2 quad processor and 8GB RAM)[66]. Docking was conducted with an X-ray crystal structure of salicyl-AMP ligase (PDB ID: 5KEI)[17b] downloaded from Protein Data Bank (www.rcsb.org).[67] The protein structure was prepared by manual removal of water molecules, merging non-polar hydrogen atoms, and computing Gasteiger charge with assigning AD4 atom type. Ligands were prepared through the PRODRG webserver (http://davapc1.bioch.dundee.ac.uk/cgi-bin/prodrg). Grid parameter files (.gpf) and docking parameter files (.dpf) were written using MGLTools-1.5.6. Receptor grids were generated using Grid points in xyz co-ordinate 60 × 60 × 60 with grid spacing of 0.375 Å. The grid box was centered on Lys546. Map types were generated using autogrid-4.2. Docking was carried out with following parameters: number of runs: 50, population size: 150, number of evaluations: 2,500,000 and number of generations: 27,000, using AutoDock4.2. Analysis of docking results was done using MGLTools-1.5.6.

Molecular dynamics. Coordinates of the MbtA enzyme (PDB ID: 5KEI)[17b] from *M. smegmatis* were obtained from the protein data bank (www.rcsb.org).[67] Missing residues (152-156 and 314-320) were modelled using the Swiss-Model server (https://swissmodel.expasy.org/interactive).[68] Water molecules from the crystal structure were manually removed. Molecular dynamics (MD)[69] simulations were performed using the GROMACS software suite (version 2019.4),[70] with OPLS-AA/L all-atom force field,[71] on an Ubuntu operating system (version 18.04).[72] The TIP4P water model[73] was used to conduct the MD simulations in explicit solvation. PACKMOL[74] was used to calculate the dimensions of the rectangular box used for simulations and the number of ions required to maintain a neutralized solution with physiological NaCl concentration of 0.16 M. The rectangular box dimensions for periodic boundary condition while keeping a minimum distance from any atom to the boundary of the box at 1 nm, were calculated to be 8.6 nm x 8.6 nm x 8.4 nm. The ligand structure was obtained from the AutoDock output file, and the hydrogens were added to the structure using Avogadro.[75] The charge parameters of the ligand were obtained from the online LigParGen webserver.[76] The system was neutralized using 49 Na^+ atoms and 29 Cl^- atoms. Steepest descent algorithm was used for energy minimizations, and maximum force F_{max} was set not to exceed 1000 kJ mol^{-1} nm^{-1}. The system was equilibrated with temperature 300K and pressure 1 bar by two consecutive 1000 ps simulations with canonical NVT ensembles and isobaric NPT ensembles, respectively.[77] Protein MbtA and inhibitors **44** and **49** were coupled together for position restraint and thermostat coupling. Molecular dynamics simulations were

run for 50 ns with stable temperature and pressure with a time step of 2 fs and long-range interaction cut-off of 1 nm. Trajectories were analyzed using inbuilt tools in the GROMACS package. The snapshots were visualized using PyMOL.[78]

The g_mmpbsa tool was used to calculate the binding free energies of the protein-ligand system.[79] A linear equation was used to solve the Poisson-Boltzmann equation to calculate the polar part of the solvation energy.[80] Solvent accessible surface area (SASA)[81] was used to calculate the nonpolar part of the solvation energy. The surface tension constant (γ) was set at 0.0226778 kJ $mol^{-1}Å^{-2}$, and the SASA constant for fitting was set at 3.84928 kJ mol^{-1}. Binding energies were extracted using the MmPbSaStat.py script and residue-specific contributions towards binding were obtained from the MmPbSaDecomp.py script. From the original MD trajectory of 50 ns, a shorter trajectory, consisting of the data from 40 to 50 ns, was used for the MM/PBSA calculations,[79] where trajectory parameters were stored for every 50 ps.

Whole-cell drug efflux pump inhibition assay.

The assay was performed using early log phase cells of *M. smegmatis* (OD_{600} ~ 0.4) and compounds were tested at sub MIC concentration (1/4 x MIC) to ensure unaltered cell viability. Cells were collected by centrifugation and resuspended in an equivalent volume of 1x PBS. The test samples comprised bacterial culture 10^7 bacteria/mL in PBS along with 0.4% glucose as the source of energy for efflux pump activity. 0.5 mg/L ethidium bromide was used as the substrate for efflux pumps, and verapamil and chlorpromazine were used as the positive controls at a concentration of 125 μg/mL. The experiment was performed in a 96-well plate that was placed in a fluorimeter and the instrument was programmed with following parameters: excitation 544 nm, emission 590 nm, cycle of measurement every minute for total period of 45 min at 37 ºC.

ASSOCIATED CONTENT

Supporting Information

The supporting information comprises:

a. Chemical characterization of intermediate chalcones.
b. X-ray crystallography parameters of compounds **44** and **49**.
c. Molecular docking study analysis.
d. MMPBSA study and analysis.
e. ^{1}H-NMR, ^{13}C-NMR, ESI-MS and HRMS spectra of analogues (**1**-**49**).
f. HPLC traces for lead compounds **44** and **49**.
g. Molecular Biology: Expression and Purification of Bimodular System.

h. Study of the effect of ligands **1**, **44**, and **49** on MbtA thermostability compared to the control 1% DMSO.
i. Mycobacterial killing by **44** and **49** inside infected macrophages.
j. *In vivo* pharmacokinetic study of **44** and **49**.
k. References.
l. Molecular Formula Strings File for analogues (**1**-**49**) as data sheet in .csv format.

Accession Codes

CCDC 2056171 and 2056172 (www.ccdc.cam.ac.uk/data_request/cif) contain the supplementary X-ray crystallographic information of **44** and **49**.

AUTHOR INFORMATION

Corresponding Author(s)

VJ; Email: venkatessanj@bitmesra.ac.in; Tel: +91-9470137264

SB; Email: s.bhakta@bbk.ac.uk /sanjib.bhakta@ucl.ac.uk; Tel: +44-2076316355

Author Contributions

VJ conceived the overall project. VJ and SB coordinated, designed and supervised the multidisciplinary project. MS performed chemical synthesis-analysis ^{1}H-NMR, ^{13}C-NMR, ESI-MS and HRMS, Hirshfeld Surface Analysis of leads, Molecular Docking, Microbiological Assays (Drug Susceptibility Testing in *M. smegmatis*, *M. aurum*, *M. bovis* BCG, Investigation of Bacteriostatic/Bactericidal mode-of-action by using HT-SPOTi method, Siderophore Production Estimation, Efflux-pump Assay, and Checkerboard Assay), MbtA Expression and Purification, Thermofluorimetry Study, Cytotoxicity, Mycobacterial killing inside infected macrophages. HV designed MbtB cloning, expression in LB medium and protein purification followed by further expression checking of MbtB clone in AI medium and protein purification was performed by MS. GB performed MD simulation and MMPBSA studies of the docked complexes. Drug-susceptibility testing in Mtb was jointly performed by MS, PM and SS. MS developed crystals of the lead candidates, followed by crystal data solving by SK. HPLC purity checking of lead candidates performed by RD. PK-profiles generated in Advinus Limited, Bangalore. FB provided the MbtA clone. MS analysed all the results and VJ, SB, CB, RD, PM, SS, PJ, SD, AKD, AS, AM, ADG, AD, BNS helped in interpreting the results. MS wrote the first complete draft of the manuscript. All the authors contributed significantly to improve the

clarity and quality of the original research presentation. The funders had no role in study design, data collection and analysis, decision to publish or preparation of the manuscript.

Notes

The authors declare no competing financial interest.

FUNDING

VJ, AD, and MS acknowledge the Department of Science and Technology Science and Engineering Research Board (DST-SERB File. No: EMR/2016/000675 dt. 05/08/2016). MS is a Newton-Bhabha International Fellow (BT/IN/NBPP/MS/20/2019-20 dt. 04/03/2020). SB acknowledges the Global Challenges Research Fund (GCRF 105123-11) for the financial support in building a UK-India capacity for tackling antimicrobial drug resistance in tuberculosis. PM gratefully acknowledges DBT-RA Program in Biotechnology and Life Sciences.

ACKNOWLEDGEMENT

Authors are thankful to Dr. Dimitrios Evangelopoulos, University College London for providing gDNA of *M. tuberculosis H37Rv.*

ABBREVIATIONS USED

CAS, chrome azurol S; CET, Conditionally Essential Target; DAP, Diaryl-substituted pyrazoline; EBFE, Estimated binding free energy; EP, Efflux pump; EPI, Efflux pump inhibitor; FBS, fetal bovine serum; GAST medium, glycerol-alanine-salts medium; $GIC_{50,}$ 50% growth inhibitory concentration; MDR, multi-drug resistance; MmpL, Mycobacterial membrane protein large; MMPBSA, Molecular Mechanics Poisson-Boltzmann Surface Area; NRPS, nonribosomal peptides synthetases; $OD_{600,}$ optical density at 600 nm; PKS, polyketide synthase; PDB, protein data bank; REMA, resazurin microtitre assay; SI, selectivity index; TSI, Target Selectivity Index; XDR, extremely-drug resistance.

REFERENCES

1. Raviglione, M. C. The TB epidemic from 1992 to 2002. *Tuberculosis* **2003**, *83*, 4-14.
2. Harding, E. WHO global progress report on tuberculosis elimination. *Lancet Respir. Med.* **2020**, *8*, 19.

3. Chan, E. D.; Laurel, V.; Strand, M. J.; Chan, J. F.; Huynh, M.-L. N.; Goble, M.; Iseman, M. D. Treatment and outcome analysis of 205 patients with multidrug-resistant tuberculosis. *Am. J. Respir. Crit. Care Med.* **2004**, *169*, 1103-1109.
4. Caminero, J. Treatment of multidrug-resistant tuberculosis: Evidence and controversies. *Int. J. Tuberc. Lung Dis.* **2006**, *10*, 829-837.
5. Eker, B.; Ortmann, J.; Migliori, G. B.; Sotgiu, G.; Muetterlein, R.; Centis, R.; Hoffmann, H.; Kirsten, D.; Schaberg, T.; Ruesch-Gerdes, S. Multidrug-and extensively drug-resistant tuberculosis, Germany. *Emerg. Infect. Dis.* **2008**, *14*, 1700.
6. Migliori, G.; Loddenkemper, R.; Blasi, F.; Raviglione, M. 125 years after Robert Koch's discovery of the tubercle bacillus: The new XDR-TB threat. Is "science" enough to tackle the epidemic? *Eur. Respir. J.* **2007**, *29*, 423-427.
7. Mitnick, C. D.; Shin, S. S.; Seung, K. J.; Rich, M. L.; Atwood, S. S.; Furin, J. J.; Fitzmaurice, G. M.; Alcantara Viru, F. A.; Appleton, S. C.; Bayona, J. N. Comprehensive treatment of extensively drug-resistant tuberculosis. *N. Engl. J. Med.* **2008**, *359*, 563-574.
8. Velayati, A. A.; Farnia, P.; Masjedi, M. R. The totally drug resistant tuberculosis (TDR-TB). *Int. J. Clin. Exp. Med.* **2013**, *6*, 307.
9. Vergne, A. F.; Walz, A. J.; Miller, M. J. Iron chelators from mycobacteria (1954–1999) and potential therapeutic applications. *Nat. Prod. Rep.* **2000**, *17*, 99-116.
10. Ratledge, C. Iron, mycobacteria and tuberculosis. *Tuberculosis* **2004**, *84*, 110-130.
11. Quadri, L. E. Strategic paradigm shifts in the antimicrobial drug discovery process of the 21st century. *Infect. Disord. Drug Targets* **2007**, *7*, 230-237.
12. Ratledge, C.; Patel, P. V.; Mundy, J. Iron transport in *Mycobacterium smegmatis*: The location of mycobactin by electron microscopy. *Microbiology* **1982**, *128*, 1559-1565.
13. Sharman, G. J.; Williams, D. H.; Ewing, D. F.; Ratledge, C. Determination of the structure of exochelin MN, the extracellular siderophore from *Mycobacterium neoaurum*. *Chem. Biol.* **1995**, *2*, 553-561.
14. Snow, G. A. Mycobactins: Iron-chelating growth factors from mycobacteria. *Bacteriol. Rev.* **1970**, *34*, 99.
15. De Voss, J. J.; Rutter, K.; Schroeder, B. G.; Barry, C. E. Iron acquisition and metabolism by mycobacteria. *J. Bacteriol.* **1999**, *181*, 4443-4451.
16. Quadri, L. E.; Sello, J.; Keating, T. A.; Weinreb, P. H.; Walsh, C. T. Identification of a *Mycobacterium tuberculosis* gene cluster encoding the biosynthetic enzymes for assembly of the virulence-conferring siderophore mycobactin. *Chem. Biol.* **1998**, *5*, 631-645.
17. (a) Ferreras, J. A.; Ryu, J.-S.; Di Lello, F.; Tan, D. S.; Quadri, L. E. Small-molecule inhibition of siderophore biosynthesis in *Mycobacterium tuberculosis* and *Yersinia pestis*. *Nat. Chem. Biol.* **2005**, *1*, 29-32. (b) Vergnolle, O.; Xu, H.; Tufariello, J. M.; Favrot, L.; Malek, A. A.; Jacobs Jr, W. R.; Blanchard, J. S. Post-translational acetylation of MbtA modulates mycobacterial siderophore biosynthesis. *J. Biol. Chem.* **2016**, *291*, 22315-22326.
18. De Voss, J. J.; Rutter, K.; Schroeder, B. G.; Su, H.; Zhu, Y.; Barry, C. E. The salicylate-derived mycobactin siderophores of *Mycobacterium tuberculosis* are essential for growth in macrophages. *Proc. Natl. Acad. Sci.* **2000**, *97*, 1252-1257.
19. Shyam, M.; Shilkar, D.; Verma, H.; Dev, A.; Sinha, B. N.; Brucoli, F.; Bhakta, S.; Jayaprakash, V. The mycobactin biosynthesis pathway: A prospective therapeutic target in the battle against tuberculosis. *J. Med. Chem.* **2020**, *64*, 71-100.
20. Stirrett, K. L.; Ferreras, J. A.; Jayaprakash, V.; Sinha, B. N.; Ren, T.; Quadri, L. E. Small molecules with structural similarities to siderophores as novel antimicrobials against *Mycobacterium tuberculosis* and *Yersinia pestis*. *Bioorg. Med. Chem. Lett.* **2008**, *18*, 2662-2668.
21. Ferreras, J. A.; Gupta, A.; Amin, N. D.; Basu, A.; Sinha, B. N.; Worgall, S.; Jayaprakash, V.; Quadri, L. E. N. Chemical scaffolds with structural similarities to

siderophores of nonribosomal peptide–polyketide origin as novel antimicrobials against *Mycobacterium tuberculosis* and *Yersinia pestis*. *Bioorg. Med. Chem. Lett.* **2011**, *21*, 6533-6537.
22. McMahon, M. D.; Rush, J. S.; Thomas, M. G. Analyses of MbtB, MbtE, and MbtF suggest revisions to the mycobactin biosynthesis pathway in *Mycobacterium tuberculosis*. *J. Bacteriol.* **2012**, *194*, 2809.
23. Lipinski, C. A. Bioisosterism in drug design. *Annu. Rep. Med. Chem.* **1986**, *21*, 283-291.
24. Falkinham III, J. O. Challenges of NTM drug development. *Front. Microbiol.* **2018**, *9*, 1613.
25. Evangelopoulos, D.; Bhakta, S. Rapid methods for testing inhibitors of mycobacterial growth. In *Antibiotic Resistance Protocols*, Springer: **2010**, 193-201.
26. Jones, C. M.; Niederweis, M. Role of porins in iron uptake by *Mycobacterium smegmatis*. *J. Bacteriol.* **2010**, *192*, 6411-6417.
27. Ferguson, L.; Wells, G.; Bhakta, S.; Johnson, J.; Guzman, J.; Parish, T.; Prentice, R. A.; Brucoli, F. Integrated target-based and phenotypic screening approaches for the identification of anti-tubercular agents that bind to the mycobacterial adenylating enzyme MbtA. *ChemMedChem* **2019**, *14*, 1735.
28. Senisterra, G.; Chau, I.; Vedadi, M. Thermal denaturation assays in chemical biology. *Assay Drug Dev. Technol.* **2012**, *10*, 128-136.
29. Huynh, K.; Partch, C. L. Analysis of protein stability and ligand interactions by thermal shift assay. *Curr. Protoc. Protein Sci.* **2015**, *79*, 28.9. 1-28.9. 14.
30. Vergnolle, O.; Xu, H.; Tufariello, J. M.; Favrot, L.; Malek, A. A.; Jacobs, W. R.; Blanchard, J. S. Post-translational acetylation of MbtA modulates mycobacterial siderophore biosynthesis. *J. Biol. Chem.* **2016**, *291*, 22315-22326.
31. Reger, A. S.; Carney, J. M.; Gulick, A. M. Biochemical and crystallographic analysis of substrate binding and conformational changes in acetyl-CoA synthetase. *Biochemistry* **2007**, *46*, 6536-6546.
32. Gulick, A. M. Conformational dynamics in the Acyl-CoA synthetases, adenylation domains of non-ribosomal peptide synthetases, and firefly luciferase. *ACS Chem. Biol.* **2009**, *4*, 811-827.
33. Brennan, P. J.; Nikaido, H. The envelope of mycobacteria. *Annu. Rev. Biochem.* **1995**, *64*, 29-63.
34. Viljoen, A.; Dubois, V.; Girard-Misguich, F.; Blaise, M.; Herrmann, J. L.; Kremer, L. The diverse family of MmpL transporters in mycobacteria: From regulation to antimicrobial developments. *Mol. Microbiol.* **2017**, *104*, 889-904.
35. Tekaia, F.; Gordon, S.; Garnier, T.; Brosch, R.; Barrell, B.; Cole, S. Analysis of the proteome of *Mycobacterium tuberculosis in silico*. *Tuberc. Lung Dis.* **1999**, *79*, 329-342.
36. Recht, J.; Kolter, R. Glycopeptidolipid acetylation affects sliding motility and biofilm formation in *Mycobacterium smegmatis*. *J. Bacteriol.* **2001**, *183*, 5718-5724.
37. Brennan, P. J.; Mayer, H.; Aspinall, G. O.; Nam Shin, J. E. Structures of the glycopeptidolipid antigens from serovars in the *Mycobacterium avium*/ *Mycobacterium intracellulare*/ *Mycobacterium scrofulaceum* serocomplex. *Eur. J. Biochem.* **1981**, *115*, 7-15.
38. López-Marín, L. M.; Gautier, N.; Lanéelle, M.-A.; Silve, G.; Daffé, M. Structures of the glycopeptidolipid antigens of *Mycobacterium abscessus* and *Mycobacterium chelonae* and possible chemical basis of the serological cross-reactions in the *Mycobacterium fortuitum* complex. *Microbiology* **1994**, *140*, 1109-1118.
39. Wells, R. M.; Jones, C. M.; Xi, Z.; Speer, A.; Danilchanka, O.; Doornbos, K. S.; Sun, P.; Wu, F.; Tian, C.; Niederweis, M. Discovery of a siderophore export system essential for virulence of *Mycobacterium tuberculosis*. *PLoS Pathog.* **2013**, *9*, e1003120.

40. Jones, C. M.; Wells, R. M.; Madduri, A. V.; Renfrow, M. B.; Ratledge, C.; Moody, D. B.; Niederweis, M. Self-poisoning of *Mycobacterium tuberculosis* by interrupting siderophore recycling. *Proc. Natl. Acad. Sci.* **2014**, *111*, 1945-1950.
41. Johnson, E. O.; Office, E.; Kawate, T.; Orzechowski, M.; Hung, D. T. Large-scale chemical-genetic strategy enables the design of antimicrobial combination chemotherapy in mycobacteria. *ACS Infect. Dis.* **2019**, *6*, 56-63.
42. Kumar, M.; Singh, K.; Naran, K.; Hamzabegovic, F.; Hoft, D. F.; Warner, D. F.; Ruminski, P.; Abate, G.; Chibale, K. Design, synthesis, and evaluation of novel hybrid efflux pump inhibitors for use against *Mycobacterium tuberculosis*. *ACS Infect. Dis.* **2016**, *2*, 714-725.
43. Solnier, J.; Martin, L.; Bhakta, S.; Bucar, F. Flavonoids as novel efflux pump inhibitors and antimicrobials against both environmental and pathogenic intracellular mycobacterial species. *Molecules* **2020**, *25*, 734.
44. Bhakta, S.; Scalacci, N.; Maitra, A.; Brown, A. K.; Dasugari, S.; Evangelopoulos, D.; McHugh, T. D.; Mortazavi, P. N.; Twist, A.; Petricci, E. Design and synthesis of 1-((1, 5-bis (4-chlorophenyl)-2-methyl-1 H-pyrrol-3-yl) methyl)-4-methylpiperazine (BM212) and N-adamantan-2-yl-N′-((E)-3, 7-dimethylocta-2, 6-dienyl) ethane-1, 2-diamine (SQ109) pyrrole hybrid derivatives: Discovery of potent antitubercular agents effective against multidrug-resistant mycobacteria. *J. Med. Chem.* **2016**, *59*, 2780-2793.
45. Andries, K.; Villellas, C.; Coeck, N.; Thys, K.; Gevers, T.; Vranckx, L.; Lounis, N.; de Jong, B. C.; Koul, A. Acquired resistance of *Mycobacterium tuberculosis* to bedaquiline. *PLoS One* **2014**, *9*, e102135.
46. Sacksteder, K. A.; Protopopova, M.; Barry, C. E.; Andries, K.; Nacy, C. A. Discovery and development of SQ109: A new antitubercular drug with a novel mechanism of action. *Future Microbiol.* **2012**, *7*, 823-837.
47. Milano, A.; Pasca, M. R.; Provvedi, R.; Lucarelli, A. P.; Manina, G.; Ribeiro, A. L. d. J. L.; Manganelli, R.; Riccardi, G. Azole resistance in *Mycobacterium tuberculosis* is mediated by the MmpS5–MmpL5 efflux system. *Tuberculosis* **2009**, *89*, 84-90.
48. Agre, N.; Khambete, M.; Maitra, A.; Gupta, A.; Munshi, T.; Bhakta, S.; Degani, M. Exploration of 5-(5-nitrothiophen-2-yl)-4, 5-dihydro-1H-pyrazoles as selective, multitargeted antimycobacterial agents. *Chem. Biol. Drug Des.* **2020**, *95*, 192-199.
49. Gupta, A.; Kaul, A.; Tsolaki, A. G.; Kishore, U.; Bhakta, S. *Mycobacterium tuberculosis*: Immune evasion, latency and reactivation. *Immunobiology* **2012**, *217*, 363-374.
50. O'Brien, R. J. Scientific blueprint for tuberculosis drug development (Global alliance for TB drug development). *Tuberculosis* **2001**, *81*, 1-52.
51. Gupta, A.; Bhakta, S. An integrated surrogate model for screening of drugs against *Mycobacterium tuberculosis*. *J. Antimicrob. Chemother.* **2012**, *67*, 1380-1391.
52. Gordien, A. Y.; Gray, A. I.; Franzblau, S. G.; Seidel, V. Antimycobacterial terpenoids from *Juniperus communis* L.(Cuppressaceae). *J. Ethnopharmacol.* **2009**, *126*, 500-505.
53. O'Donnell, G.; Gibbons, S. Antibacterial activity of two canthin-6-one alkaloids from *Allium neapolitanum*. *Phytother. Res.* **2007**, *21*, 653-657.
54. Carvalho, R.; de Sonneville, J.; Stockhammer, O. W.; Savage, N. D.; Veneman, W. J.; Ottenhoff, T. H.; Dirks, R. P.; Meijer, A. H.; Spaink, H. P. A high-throughput screen for tuberculosis progression. *PLoS One* **2011**, *6*, e16779.
55. Khan, A.; Sarkar, D. A simple whole cell based high throughput screening protocol using *Mycobacterium bovis* BCG for inhibitors against dormant and active tubercle bacilli. *J. Microbiol. Methods* **2008**, *73*, 62-68.
56. Naik, S. K.; Mohanty, S.; Padhi, A.; Pati, R.; Sonawane, A. Evaluation of antibacterial and cytotoxic activity of *Artemisia nilagirica* and *Murraya koenigii* leaf extracts against mycobacteria and macrophages. *BMC Complement. Altern. Med.* **2014**, *14*, 1-10.

57. Lun, S.; Guo, H.; Adamson, J.; Cisar, J. S.; Davis, T. D.; Chavadi, S. S.; Warren, J. D.; Quadri, L. E.; Tan, D. S.; Bishai, W. R. Pharmacokinetic and *in vivo* efficacy studies of the mycobactin biosynthesis inhibitor salicyl-AMS in mice. *Antimicrob. Agents Chemother.* **2013**, *57*, 5138-5140.
58. Bruker. APEX, APEX2, SMART, SAINT and SAINT-Plus. In Bruker AXS Inc.: Madison, Wisconsin, USA, **2012**.
59. Sheldrick, G. M. SADABS, An empirical absorption correction program, Madison. In Bruker Analytical X-ray Systems: WI: **1996**.
60. Sheldrick, G. M. Crystal structure refinement with SHELXL. *Acta Crystallogr. Sec. C* **2015**, *71*, 3-8.
61. Farrugia, L. J. WinGX and ORTEP for Windows: An update. *J. Appl. Crystallogr.* **2012**, *45*, 849-854.
62. Spackman, M. A.; Jayatilaka, D. Hirshfeld surface analysis. *CrystEngComm* **2009**, *11*, 19-32.
63. Molla, A.; Ranjan, S.; Rao, M. S.; Dar, A. H.; Shyam, M.; Jayaprakash, V.; Hussain, S. Borax catalysed domino synthesis of highly functionalised spirooxindole and chromenopyridine derivatives: X-Ray structure, hirshfeld surface analysis and molecular docking studies. *ChemistrySelect* **2018**, *3*, 8669-8677.
64. Mori, M.; Stelitano, G.; Gelain, A.; Pini, E.; Chiarelli, L. R.; Sammartino, J. C.; Poli, G.; Tuccinardi, T.; Beretta, G.; Porta, A. Shedding X-ray light on the role of magnesium in the activity of *Mycobacterium tuberculosis* salicylate synthase (MbtI) for drug design. *J. Med. Chem.* **2020**, *63*, 7066-7080.
65. Danquah, C. A.; Maitra, A.; Gibbons, S.; Faull, J.; Bhakta, S. HT-SPOTi: A rapid drug susceptibility test (DST) to evaluate antibiotic resistance profiles and novel chemicals for anti-infective drug discovery. *Curr. Protoc. Microbiol.* **2016**, *40*, 17-8.
66. Morris, G. M.; Huey, R.; Lindstrom, W.; Sanner, M. F.; Belew, R. K.; Goodsell, D. S.; Olson, A. J. AutoDock4 and AutoDockTools4: Automated docking with selective receptor flexibility. *J. Comput. Chem.* **2009**, *30*, 2785-2791.
67. Berman, H. M.; Westbrook, J.; Feng, Z.; Gilliland, G.; Bhat, T. N.; Weissig, H.; Shindyalov, I. N.; Bourne, P. E. The protein data bank. *Nucleic Acids Res.* **2000**, *28*, 235-242.
68. Guex, N.; Peitsch, M. C. SWISS-MODEL and the SWISS-PDB Viewer: An environment for comparative protein modeling. *Electrophoresis* **1997**, *18*, 2714-2723.
69. Karplus, M.; Petsko, G. A. Molecular dynamics simulations in biology. *Nature* **1990**, *347*, 631-639.
70. Abraham, M. J.; Murtola, T.; Schulz, R.; Páll, S.; Smith, J. C.; Hess, B.; Lindahl, E. GROMACS: High performance molecular simulations through multi-level parallelism from laptops to supercomputers. *SoftwareX* **2015**, *1*, 19-25.
71. Jiang, F.; Zhou, C.-Y.; Wu, Y.-D. Residue-specific force field based on the protein coil library. RSFF1: Modification of OPLS-AA/L. *J. Phys. Chem. B* **2014**, *118*, 6983-6998.
72. Helmke, M. *Ubuntu Unleashed 2019 Edition: Covering 18.04, 18.10, 19.04*. Addison-Wesley Professional: **2018**.
73. Horn, H. W.; Swope, W. C.; Pitera, J. W.; Madura, J. D.; Dick, T. J.; Hura, G. L.; Head-Gordon, T. Development of an improved four-site water model for biomolecular simulations: TIP4P-Ew. *J. Chem. Phys.* **2004**, *120*, 9665-9678.
74. Martínez, L.; Andrade, R.; Birgin, E. G.; Martínez, J. M. PACKMOL: A package for building initial configurations for molecular dynamics simulations. *J. Comput. Chem.* **2009**, *30*, 2157-2164.
75. Hanwell, M. D.; Curtis, D. E.; Lonie, D. C.; Vandermeersch, T.; Zurek, E.; Hutchison, G. R. Avogadro: An advanced semantic chemical editor, visualization, and analysis platform. *J. Chemoinformatics* **2012**, *4*, 1-17.

76. Dodda, L. S.; Cabeza de Vaca, I.; Tirado-Rives, J.; Jorgensen, W. L. LigParGen web server: An automatic OPLS-AA parameter generator for organic ligands. *Nucleic Acids Res.* **2017**, *45*, W331-W336.
77. Tan, S. J.; Prasetyo, L.; Zeng, Y.; Do, D.; Nicholson, D. On the consistency of NVT, NPT, μVT and Gibbs ensembles in the framework of kinetic Monte Carlo–Fluid phase equilibria and adsorption of pure component systems. *Chem. Engg. J.* **2017**, *316*, 243-254.
78. DeLano, W. L.; Bromberg, S. PyMOL user's guide. *DeLano Scientific LLC* **2004**, 629.
79. Kumari, R.; Kumar, R.; Consortium, O. S. D. D.; Lynn, A. g_mmpbsa-A GROMACS tool for high-throughput MM-PBSA calculations. *J. Chem. Inf. Model.* **2014**, *54*, 1951-1962.
80. Fogolari, F.; Brigo, A.; Molinari, H. The Poisson-Boltzmann equation for biomolecular electrostatics: A tool for structural biology. *J. Mol. Recognit.* **2002**, *15*, 377-392.
81. Richmond, T. J. Solvent accessible surface area and excluded volume in proteins: Analytical equations for overlapping spheres and implications for the hydrophobic effect. *J. Mol. Biol.* **1984**, *178*, 63-89.

Table of Contents graphic:

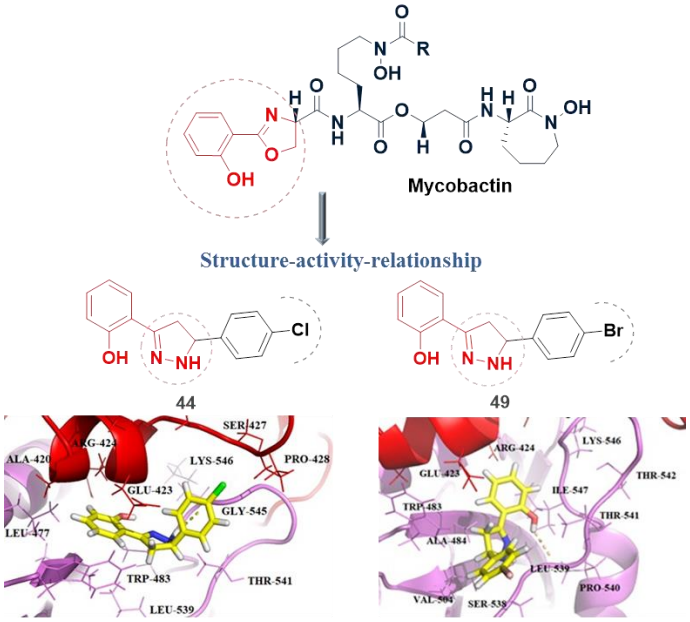

✓ Bind and inhibit Salicyl-AMP Ligase

✓ Antimicrobial activities against Mtb and NTM

✓ Affect intracellular survival of mycobacteria

✓ Inhibit whole-cell drug efflux pumps

✓ Excellent PK profile